



UNIVERSIDAD DE CHILE
FACULTAD DE CIENCIAS FÍSICAS Y MATEMÁTICAS
DEPARTAMENTO DE FÍSICA

**ESTUDIO DEL EFECTO ELECTROADSORTIVO EN PELÍCULAS DE
ÓXIDO DE ESTAÑO**

TESIS PARA OPTAR AL GRADO DE MAGÍSTER EN CIENCIAS, MENCIÓN FÍSICA

ANTONIO ALFREDO IBÁÑEZ LANDETA

PROFESOR GUÍA:
VICTOR FUENZALIDA ESCOBAR

MIEMBROS DE LA COMISIÓN:
DONOVAN DÍAZ DROGUETT
THEODOR DOLL
MARCOS FLORES CARRASCO

Este trabajo ha sido parcialmente financiado por Proyecto ACT1117,
Beca de Magíster Nacional CONICYT,
FONDECYT regular 1140759

SANTIAGO DE CHILE
2017

ABSTRACT OF THE THESIS FOR THE DEGREE OF: Magíster en Ciencias, mención Física
BY: Antonio Ibáñez Landeta
DATE: 01/03/2017
SUPERVISOR: Victor Fuenzalida Escobar

STUDY OF THE ELECTROADSORPTIVE EFFECT ON A TIN DIOXIDE FILM

Electroadsorption is the adsorption of a gas on a surface, stimulated or inhibited by the offer or depletion of electrons at the surface, caused by an electric field. The electroadsorption of NO_2 from a NO_2 - O_2 mixture on a tin oxide surface and the identification of the chemical states on the surface were the object of this thesis.

The experimental work required the design and implementation of a special chamber dedicated to the electroadsorption process. The experimental set-up allows a sample to be polarized at different voltages under ultra-high vacuum conditions, and is able to allow transferring the sample without interrupting the polarization from the adsorption chamber to the analysis chamber, where the measurements can be performed under polarization. The adsorption chamber can be filled with a NO_2 - O_2 mixture, which is obtained via thermal decomposition of lead nitrate $\text{Pb}(\text{NO}_3)_2$. A mass spectrometer allows monitoring the composition of the gases at all times. The samples were prepared by RF-assisted sputtering of SnO_2 in a O_2 /Ar atmosphere onto a silicon wafer with 100 nm. of thermal oxide, followed by thermal treatment at 400°C during 10 hours in a synthetic air atmosphere. The resulting wafer was cut into 10×12 mm rectangular pieces. A thin (around 100 nm.) copper “C” shaped contact was evaporated on top while aluminum was evaporated onto the back in order to use the metals as electrical contacts to polarize the sample. The conditions, namely polarity and magnitude, of the applied potential which allow the SnO_2 surface to be equipotential were determined using surface potential measurements with a multimeter as well as X-ray photoelectron spectrometry (XPS) to detect shifts of the XPS signals.

Using the aforementioned chamber, the electroadsorptive effect of NO_2 on SnO_2 was investigated by applying voltages at the back, from -15 V to + 15 V while the surface was grounded. XPS measurements revealed elemental nitrogen as well as nitrogen oxides (NO_3 and NO_2) on the metal oxide surface. The application of negative back potentials inhibited the adsorption of nitrogen oxides, while the application of positive back potentials promoted it. The adsorption of elemental nitrogen is not affected in any case.

RESUMEN DE LA TESIS PARA OBTAR AL
GRADO DE: Magíster en Ciencias, mención Física
POR: Antonio Ibáñez Landeta
FECHA: 01/03/2017
PROFESOR GUÍA: Victor Fuenzalida Escobar

ESTUDIO DEL EFECTO ELECTROADSORPTIVO EN PELÍCULAS DE ÓXIDO DE ESTAÑO

El efecto electroadsorptivo es la adsorción de gas sobre una superficie sólida estimulada o inhibida por la acción de un campo eléctrico, el que modifica la densidad de electrones en la superficie. Esta tesis estudió el efecto electroadsorptivo de una mezcla gaseosa de $\text{NO}_2\text{-O}_2$ sobre una superficie de óxido de estaño.

El experimento requirió del diseño e implementación de una cámara de vacío dedicada al proceso de electroadsorción. El montaje hace posible que una muestra sea polarizada a distintos voltajes en condiciones de alto vacío, permitiendo transferir la muestra (sin interrumpir la polarización) desde la cámara de adsorción a la cámara de análisis de espectroscopia de fotoelectrones (XPS) para realizar las mediciones. La cámara de adsorción puede inundarse con una mezcla gaseosa de $\text{NO}_2\text{-O}_2$ obtenida por descomposición térmica de nitrato de plomo $\text{Pb}(\text{NO}_3)_2$. Un espectrómetro de masas permite la monitorización de la composición de los gases en cualquier instante.

Las muestras fueron preparadas por *sputtering* asistido por radiofrecuencia. Se usó un blanco de SnO_2 en una atmósfera de O_2/Ar . El material fue depositado en una oblea de silicio con 100 nm de óxido térmico, seguido de un tratamiento térmico a 400°C durante 10 horas en atmósfera de aire sintético. Posteriormente, la oblea fue cortada en piezas rectangulares de 10×12 mm. Un delgado (100 nm de espesor) contacto de cobre en forma de C fue evaporado sobre su superficie, mientras que su parte posterior fue metalizada con aluminio, creando así contactos para polarizar la muestra.

Las condiciones del potencial aplicado que permiten que la superficie del SnO_2 sea equipotencial se determinaron midiendo el potencial en la superficie con un multímetro y con XPS para detectar posibles corrimientos en la señal.

Usando la cámara previamente mencionada, se estudió el efecto electroadsorptivo del NO_2+O_2 sobre SnO_2 aplicando distintos potenciales a la parte trasera de la muestra, desde -15 V a +15 V, mientras su superficie se encontraba aterrizada. Las medidas de XPS revelaron la presencia de nitrógeno elemental, así como de óxidos de nitrógeno (NO_3 y NO_2) en la superficie del óxido metálico. La aplicación de un potencial negativo a su cara posterior inhibe la adsorción de estos óxidos, mientras que la aplicación de un potencial positivo la promueve. No se observó una modificación apreciable en la adsorción del nitrógeno elemental.

Acknowledgements

Si bien la tesis está escrita en inglés, escribo los agradecimientos en español ya que los involucrados en esta sección son principalmente hispanohablantes.

En primera instancia, me gustaría agradecer a mis padres. A lo largo de mi paso por la universidad, y de diversas formas y fuentes, me ha tocado oír que estudiar física es “condenarse a morir de hambre”. A pesar de esta idea presente en la sociedad chilena (que tiene otras implicancias que no voy a discutir acá), mis padres me dieron todo su apoyo, tanto moral como monetario, para que prosiguiera mis estudios. Los quiero, gracias.

También le agradezco al profesor Victor Fuenzalida por su trabajo como profesor guía y la paciencia con la gran cantidad de errores, tanto en el desarrollo del trabajo de tesis como en la escritura de la misma (en particular los de redacción).

Al profesor Theodor Doll por las observaciones y correcciones a lo largo del trabajo. Si bien fueron dadas de una forma ruda, al final todo es para mejor.

A Andrés, Ricardo y Cristófer por su vital trabajo en el diseño e implementación del montaje que permitió realizar esta tesis.

A Noelia Benito por su ayuda a la hora de procesar los espectros XPS y las imágenes AFM.

A la gente del laboratorio, tantos los que están como los que se han ido: Boris Chornik, Marcos Flores, Henry Fernandez, Sebastián (Bahamondes y Donoso), Pablo Cabello, Italo Moglia, Fernando Guzmán y más gente que seguro estoy olvidando. Ya sea por las conversaciones de pasillo sobre el tema, ayuda a la hora de usar los equipos o simplemente compartir un instante de relajo.

A mis amigos, compadres y compinches varios por los buenos ratos pasados todos estos años. No los menciono por nombre porque más de uno es sensible y se va a sentir si es que se me pasa anotarlos. Sepan que los aprecio a todos aunque no logre hacer una lista completa.

Al departamento de física de la FCFM por ayudarme a pagar el durante el período que no tuve beca CONICYT.

Contents

1	Introduction	1
1.1	Objectives	2
1.2	Adsorption	2
1.2.1	Physisorption	4
1.2.2	Chemisorption	4
1.3	Electroadsorptive effect	6
1.4	Other adsorbed species	9
1.5	Atomic Force Microscopy	9
1.6	Low Energy Ion Spectroscopy	10
1.7	X-ray photoelectron spectroscopy (XPS)	11
1.7.1	Time resolved measurements	12
1.8	Mass Spectrometer	12
2	Experimental setup	13
2.1	General description	13
2.1.1	Insertion arm	14
2.1.2	Sample holder	14
2.1.3	Gas Source	15
2.1.4	Mass Spectrometer	15
2.1.5	Gas atmosphere	15
2.2	Sample	16
2.2.1	Surface potential measurement	17
2.2.2	Circuit	17
2.3	Other experiments	18
2.3.1	Titanium oxide	18
2.3.2	Thiols	18
2.3.3	Topographical characterization	19
3	Results	20
3.1	Preliminary measurements	20
3.1.1	XPS spectra at $\phi = 0$	20
3.1.2	Grounding of the surface	22
3.1.3	Verification of surface contaminants	26
3.1.4	Direct measurement of the surface potential	27
3.2	Exposition to the NO ₂ /O ₂ gas mixture.	32
3.2.1	Sample never polarized	33

3.2.2	Sample polarized only during gas exposition	36
3.2.3	Sample permanently polarized	39
3.3	Additional experiments	41
3.3.1	Thiols on the SnO ₂ surface	41
3.3.2	Titanium dioxide film on the SnO ₂ surface	43
3.3.3	Topographical characterization	45
4	Discussion	46
4.1	Grounding of the surface of the sample	46
4.2	Argon erosion	47
4.3	QMA	48
4.4	NO _x and H ₂ O interaction	48
4.5	Adsorption and desorption kinetics	49
4.6	Desorption and temperature	50
4.7	Thiols on SnO ₂	50
4.8	TiO ₂ film on SnO ₂	51
4.9	Future work	51
	Conclusion	52
	Bibliography	53

List of Tables

1.1	Values for the various constants used on equation (1.6)	7
2.1	Relative percentages of gases in chamber	16
2.2	Relative percentages of gases in chamber during flooding	16
3.1	Peak positions, FWHM and chemical contribution at 0 V	22
3.2	Peak shift as function of the polarization voltage ϕ	25
3.3	Binding energy (eV) of the N 1s peaks.	33
3.4	Fitted values for the exponential function parameters. The function used was $f(t) = y_0 + A \exp(-R_0 t)$	35
3.5	N 1s, NO ₂ and NO ₃ relative % present on the sample at t=2.5 min as function of V and the current through the sample	38
3.6	Values of the fitting parameters. The function used was $f(t) = y_0 + Ae^{-R_0 t}$	40
3.7	Binding energy for each Gauss-Lorenz adjustment curve, its relative percentage compared to the whole S signal and its interpretation as found in the literature	43
3.8	Ti and Sn peak positions	44

List of Figures

1.1	Band bending for different semiconductors. a) and b) show the energy diagram for a n-type semiconductor before and after adsorption equilibrium, while c) and d) present the energy diagram for a p-type semiconductor before and after adsorption equilibrium	6
1.2	Sketch of the electroadsorptive effect for a induced electric field E pointing towards the sample bottom and b induced electric field E pointing towards the sample surface.	8
1.3	Diagram of a thiol on a substrate. The head group (red), tail group (blue) and terminal group (green) are shown.	9
1.4	Diagram of AFM working principle	10
1.5	Diagram of the geometry used for LEIS.	11
1.6	Diagram of XPS working principle	11
2.1	Experimental setup schematics	13
2.2	Side view of the insertion arm.	14
2.3	Pictures of the sample holder. The red line shows its scale.	15
2.4	Sample, right after contact evaporation	17
2.5	Sample with the point contacts used for the surface potential measurement	17
2.6	Schematics of the circuit used.	18
3.1	Survey spectrum when the sample is not polarized.	20
3.2	High resolution spectra of the non polarized sample.	21
3.3	Expected behavior for a MOS device with small contacts on top	22
3.4	Schematics of the different circuits tested	23
3.5	XPS spectra of a C 1s , b O 1s and c Cu 2p _{3/2} at different polarization ϕ values.	24
3.6	Sn 3d spectra at -15, 0 and +15 V. The pink dashed line corresponds to the Gauss-Lorenz curve used for adjustment.	26
3.7	Sn 3d spectra at -12, 0 and +12V. The pink dashed line corresponds to the Gauss-Lorenz curve used for adjustment.	26
3.8	LEIS spectra of a sample with evaporated contacts. The associated element to each peak is labelled on top.	26
3.9	Contour line plot for $\phi = -5$ (top) and $\phi = +5$ (bottom).	28
3.10	Contour line plot for $\phi = -9$ (top) and $\phi = +9$ (bottom).	29
3.11	Contour line plot for $\phi = -12$ (top) and $\phi = +12$ (bottom). The voltage is measured in mV	30
3.12	Contour line plot for $\phi = -15$ (top) and $\phi = +15$ (bottom).	31

3.13	N 1s XPS spectra recorded at a $t=2,5$ min, b $t=20$ min and c $t=42,5$ min after the measurement started.	34
3.14	Mean curve obtained for $\text{NO}_2 + \text{NO}_3$ concentration onto the SnO_2 surface as function of time. The exponential fit is shown as a red line	35
3.15	N 1s XPS spectra recorded after exposition to the gas mixture while polarized at a) $\phi = +15$ V, b) $\phi = 0$ V and c) $\phi = -15$ V.	36
3.16	N percentage as a function of initial polarization ϕ	37
3.17	NO_2 percentage as a function of initial polarization ϕ	37
3.18	NO_3 percentage as a function of initial polarization ϕ	37
3.19	$\text{NO}_2 + \text{NO}_3$ percentage as a function of initial polarization ϕ	37
3.20	N 1s XPS spectra recorded after exposition to the gas mixture while maintaining ϕ at a) $+8$ V, (b) -8 V, (c) $+15$ V, (d) -15 V.	39
3.21	$\text{NO}_2 + \text{NO}_3$ relative area as function of time at $\phi = \{\pm 8, +10, \pm 12 \text{ and } \pm 15\}$. The colored line shows the respective exponential fit.	40
3.22	XPS high-resolution spectra of the S signal on the sample right after preparation, after a $+15$ V potential was applied to the sample backside and after a -15 V potential was applied to the sample backside.	42
3.23	LEIS spectra of a sample with a 1 nm Ti film on top.	43
3.24	XPS spectra of the TiO_2 coated sample at $\phi = +15$ (red), 0 (black) and -15 V (blue)	44
3.25	AFM image of the SnO_2 sample surface before (a) and after (b) gas exposure while its back was polarized at different ϕ	45
3.26	Height histogram of a sample before (a) and after (b) gas exposure while its back was polarized at different ϕ	45
4.1	a) Highest deviation from zero surface potential as function of ϕ . b) Point where the highest deviation was found for all ϕ (area marked in blue)	46
4.2	Sketch of the proposed grid contact for grounding the surface of the sample .	47
4.3	Left: This work proposed SnO_2 surface after adsorption of NO_x species. Right: Top view of the two possible configurations for water adsorption on a saturated SnO_2 (110) surface [1].	49

Chapter 1

Introduction

The electroadsorptive effect is the modulation of a material's adsorptivity by using an electric field, that is, being able to control whether a sample surface adsorbs or desorbs a certain gas by applying an electric field perpendicular to the surface. First postulated by Wolkenstein in 1958[2], it was not further explored due to the huge field necessary (above 10^6 V/m) [3][4] to observe it. 30 years later, with the advent of micromachined devices (which are smaller and thus have stronger internal electrical fields) some adsorption changes under field alterations were observed and related to the electroadsorptive effect [5]. Regarding the theory behind the electroadsorptive effect, the Wolkenstein model was completed by Gerslinger on 1993 [6], and it describes adsorption changes under electrical field alterations, relating to the electroadsorptive effect. Using this expanded Wolkenstein model, Velasco-Velez et al developed a quantum mechanical description of coadsorption of gases when an electrical field is applied to the sample [7].

From an experimental standpoint, this phenomenon was first studied in 1997 [8] and then expanded on 1998 when a design of a hybrid suspended gate FET (HSGFET) device (consisting of a ISFET with a oxide-nitride sandwich on top and a silicon gate suspended at $1\mu m$ from the surface) was used as a sensor gas [9]. Since a suspended gate offers another surface for adsorption this has the double disadvantage that it acts as an extra desorption source one has to take into account when measuring adsorption/desorption curves and, since its so close to the reactive surface, it also acts as an extra unwanted source that complicates measuring the electroadsorptive effect on the target surface and it makes impossible in-situ surface studies. These problems are overcome by using a buried control electrode instead of a suspended one and used to directly observe for the first time the electroadsorptive effect [10]. T. Doll et. al. also proposes a tentative model for the strong chemisorption in his paper by combining both the Wolkenstein-Gerslinger model and Shockley-Read-Hall statistics.

However, no further study has been yet performed regarding the electroadsorptive effect at different voltage values, whether is a continuous effect or if there are either lower or upper thresholds for the stability of the device presented by T. Doll et. al. While there are observations and applications of the phenomenon on other works, such as the one done by M. Noked et. al. [11], not much studies have yet been done on the electroadsorptive effect on different materials (both adsorbants and adsorbates)

Tin oxide is a metal oxide semiconductor which is transparent to visible light and a electric resistivity of $\rho \approx 10^{-3}\Omega \cdot cm$ [1]. These properties make it a very attractive material for optoelectronic applications, such as transparent conductor for solar panels and fabrication of smart windows. Both its gas sensitivity and the possibility of synthesizing tin oxide nanowires and nanotapes [12] make it a good candidate for catalyst in surface oxidative reactions and as solid state gas sensor for certain gases, such as nitrogen dioxide [13].

Nitrogen dioxide (NO_2) is a strong oxidizing agent, which is formed in motor vehicle exhausts due to the high temperature involved. It reacts with either atmospheric oxygen or carbon-based molecules to form either corrosive nitric acid or toxic organic nitrates. Moreover, it plays a major role in the atmospheric reactions that produce ground-level ozone, as sunlight splits it into nitric oxide (NO) and oxygen atom, which then forms ozone by combining with diatomic oxygen. The US Environmental Protection Agency (EPA) recognizes its effects on the respiratory system by lowering the human resistance to influenza and increasing the allergenic effects of certain elements due to lung irritation. Also, some studies suggest a link between NO_2 and lung cancer[14]

Solid-state sensors principal working method consists in promoting the adsorption of the target gas by heating the sensor to temperatures above 300 °C [15][16]. This technique is not without problems: high temperature may induce some morphological changes that decrease sensor stability, while high power consumption makes them non autonomous devices and the high operational temperature makes integration to CMOS circuits difficult.

1.1 Objectives

The general objective of this thesis was to specify experimental details of the work done by Theodor et. al. on the electroadsorptive effect on a thin SnO_2 film. This was realized by using a mass spectrometer and X ray photoelectron spectroscopy. In order to accomplish this objective, the following specific objectives were pursued.

- Design and construction of a dedicated vacuum chamber annex to the XPS chamber. The chamber allows continuous voltage application on a sample mounted on a linear motion feedthrough.
- Study the conditions that ensure an equipotentially grounded surface at different back-side polarization values.
- Obtaining the adsorption and desorption rates of the sample and specify whether it adjusts to a Wolkenstein et. al. isotherm.

1.2 Adsorption

Adsorption is the adhesion of atoms or molecules (named adsorbates) to another surface (named adsorbant). This process, being a surface-based process, differs from absorption,

which involves the whole volume of the material. The "classical" adsorption theory is the one proposed by Langmuir, which is based on the following assumptions

- 1 Adsorption takes place at separate adsorption centers. Each center can only hold 1 gas molecule, and the surface has centers of only one type, characterized by a binding energy q .
- 2 The adsorbed molecules do not interact with each other.
- 3 The number of adsorption centers is constant, but it depends on the surface history. It is temperature independent and does not vary when the surface is partially covered by adsorbates.
- 4 Each adsorption center and each molecule interact only in one way.

With these assumptions in mind, we get:

$$\frac{dN}{dt} = \alpha P(N^* - N) - \beta N \quad (1.1)$$

$$\alpha = \frac{\kappa s}{\sqrt{2\pi M k T}} \quad \beta = \nu \exp\left(\frac{-q}{kT}\right)$$

Where N^* is the number of adsorption centers per unit area, s is the effective surface area, κ is the probability that a molecule sticks to the adsorption center, β is the desorption probability per unit time, ν is a characteristic frequency (estimated to be around $10^{13} \frac{1}{s}$ [17]) and q is the binding energy. P is the partial pressure of the adsorbing gas and T the temperature of the system.

The first term of the equation would be the number of molecules arriving per unit area to the adsorption centers, while the second term represents the rate of molecules leaving the surface.

For $N = 0$ at $t = 0$ we easily obtain

$$N(t) = N^* \frac{bP}{1 + bP} (1 - \exp(-(\alpha P + \beta)t)) \quad (1.2)$$

Where $b = \frac{\alpha}{\beta}$.

The desorption equation can be calculated with equation (1.1) using $P = 0$ and $N = N_0$ at $t = 0$.

$$N(t) = N_0 \exp(-\beta t) \quad (1.3)$$

However, there is usually a fraction of the adsorbate that can't be removed from the surface by lowering the pressure since it remains permanently attached to it (Partial irreversibility of adsorption). This case is not contemplated in Langmuir's theory, but the equation can be modified to represent this by adding a constant N_{irrev} :

$$N(t) = N_{irrev} + N_0 \exp(-\beta t) \quad (1.4)$$

The adsorption processes are classified as physisorption and chemisorption

1.2.1 Physisorption

Physisorption refers to the surface binding of atoms or molecules due to van der Waals or electrostatic forces. In this case, there is no electron exchange between adsorbate and adsorbent.

1.2.2 Chemisorption

Chemisorption refers to the surface binding of atoms when the electron wavefunction of adsorbate and adsorbant overlap. The strength of this bond depends on whether the chemisorbed system (molecule + adsorption center) remains electrically neutral or not, thus we can have positive, negative or neutral charged ions on the sample surface, depending of whether the adsorbed molecule acts as a donor, an acceptor or takes no electrons from the surface. If the chemisorbed particle retains in its neighborhood a charge carrier, the bond is called "strong", while the neutral form is named "weak", named so because of the relative bonding strength. In the strong case, the binding between molecule and surface may be strong enough to be irreversible.

Chemisorption at equilibrium is modelled by the Wolkenstein-Geistlinger isotherm, shown on equation (1.5).[6]

$$N = Nc^* \frac{\beta \cdot p}{\beta p + 1} \quad (1.5)$$

$$\beta = \frac{b}{f^0 \left(1 + \frac{\nu^-}{2\nu^0} \exp\left(-\frac{(E_c - E_f)}{kT}\right) \right)} \quad f^0 = \frac{1}{\frac{1}{2} \exp\left(\frac{E_f - E_s}{kT}\right) + 1}$$

Where Nc^* is the number of chemisorption centers per unit area, b is the kinetic adsorption coefficient defined in equation (1.2), f^0 the occupation probability of the weak-chemisorbed state. The factor $\frac{1}{2}$ next to the exponential function on the denominator of f_0 arises from

the spin degeneration of the single-occupied state [18]. The constants ν^0 and ν^- are the phononic frequency of weak and strong chemisorbed states respectively (both values around 10^{13} Hz), E_f the Fermi energy level and E_c the conduction band energy edge. E_s is the surface-state energy, which is calculated as the difference between the binding energies of the strong chemisorbed state (E_a) and weak chemisorbed states (E_{a0}). In this way $E_s = E_a - E_{a0}$, as defined by Geistlinger [6].

As previously mentioned, in the case of strong chemisorption the adsorbant “pins” a charge carrier to the surface. If the adsorbant acts as an acceptor, the electron concentration on the surface increases as more of them are adsorbed. This induces an upward bending of the surface bands, inhibiting the adsorption of extra molecules. In the case of donor molecules, they increase the hole concentration on the surface, inducing a downwards band bending which produces the same inhibition. This effect is known as the Weisz self-limitation, and it limits the surface coverage due to strong chemisorption to 10^{12} - 10^{13} cm^{-2} , which is less than 1% of surface coverage [19].

This is schematically shown in Figure 1.1. **a)** shows the energy diagram of a n-type semiconductor with work function Φ , Fermi energy E_f and molecules with electron affinity A . The molecules will chemically adsorb until the charge transfer has raised the Fermi level of the solid to coincide with that in the adsorbate (in an amount $E_0 = A - \Phi$) as seen on Figure 1.1 **b)**. A corresponding picture is shown in Figure 1.1 **c)** and **d)**, for a p-type semiconductor and adsorbable molecules with an ionization potential I , with resulting donation from the adsorbate until $E_0 = \Phi - I$. In both cases, the amount of adsorbed molecules would be N_0 .

It may be of use to identify two special cases of chemisorption

- Dissociative adsorption: The adsorbate dissociates into two or more fragments which are bound to the surface.
- Reactive adsorption: Which is similar to dissociative adsorption, but one fragment adsorbs to an adsorbate rather than to a surface site.

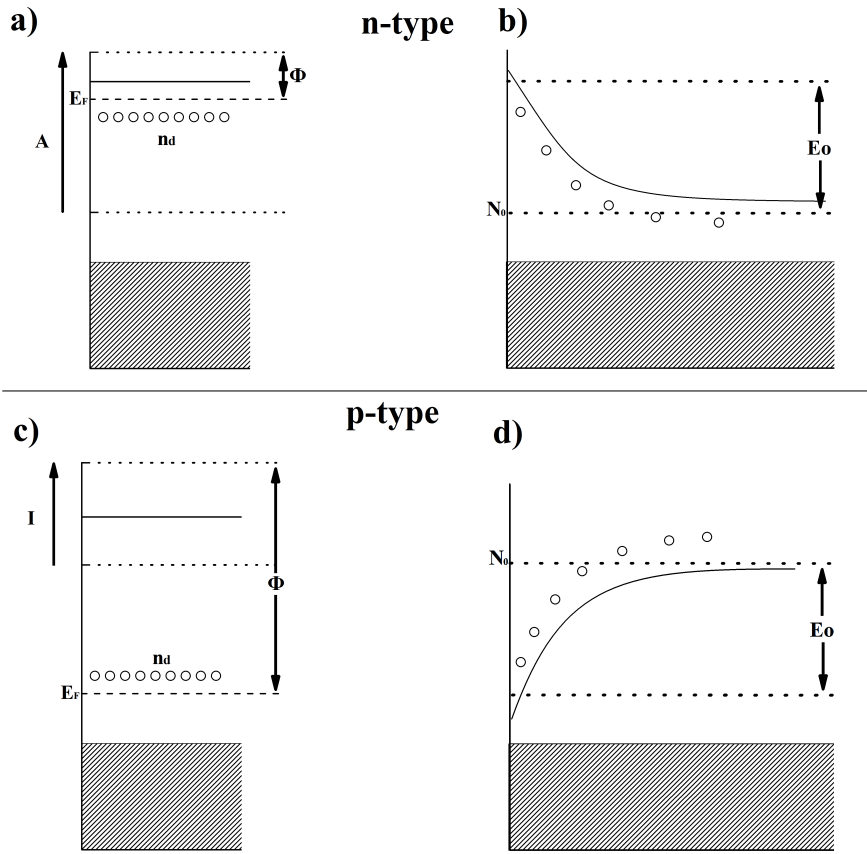


Figure 1.1: Band bending for different semiconductors. **a)** and **b)** show the energy diagram for a n-type semiconductor before and after adsorption equilibrium, while **c)** and **d)** present the energy diagram for a p-type semiconductor before and after adsorption equilibrium

1.3 Electroadsorptive effect

As previously described, the chemisorption is governed by surface transport processes, and the Wolkenstein-Geistlinger isotherm relates the surface coverage with both the Fermi level and the energy surface level. If one changes the temperature of the semiconductor layer, the statistics of surface transport processes (such as charge carrier and gas diffusion) are changed, altering the adsorption equilibrium conditions [20]. This method, however, is far from ideal as it may induce some morphological changes in the semiconductor layer. Another way to modify the adsorption statistics of a surface is to modify the surface energy bands. This can be achieved by applying an electrical field perpendicular to a semiconductor surface, thus altering the surface bands relative positions to the Fermi level. This modification of the surface adsorptivity via an applied electrical field is the so called Electroadsorptive effect. It has been recognized that high electrical fields (around 10^7 V/m) [3] [4] are needed in order to properly observe this effect. This can be achieved by using a thin layer of semiconductor material with both an electrode on the back of the substrate and a (grounded) electrode deposited on the surface.

For a semiconductor, the space charge region usually extends to only a few nanometers and thus creating an electric potential gradient. However, it has been found that if the semiconductor layer thickness is around 2 Debye screening lengths, the whole metal oxide can be greatly influenced by the electrodes on its sides [21], which allows for both modification of the surface properties via the application of an electrical potential ϕ to the back of the sample and maintaining an equipotential on the sample surface via the grounding of the deposited surface electrode (at least for moderate values of ϕ).[5] [22] [23].

In order to properly model the desorption of the strongly chemisorbed molecules as a function of time, T. Doll et. al. combined the Wolkenstein-Gestlinger isotherm with Shockley-Read-Hall statistics, describing the desorption rate by means of capture processes. The rate of desorption of the charged species is described by a capture coefficient K_n that rules over the weakly chemisorbed ones as seen on Eqn (1.6)[10]

$$\frac{dN^-}{dt} = K_n(N - N^-)N_c \exp\left(\frac{E_{cs} - E_f}{kt}\right) - N^-N_c \exp\left(-\frac{E_{cs} - E_t}{kT}\right) \quad (1.6)$$

Where N^- is the number of strong chemisorbed species per unit area and N the total number of chemisorbed species per unit area, E_f is the Fermi energy, E_{cs} is the lower band edge at the surface, E_t the energy of the trap states K_n and is the capture coefficient and $N_c = 2M_c\left(\frac{2\pi m_e^* kT}{h^2}\right)^{\frac{3}{2}}$ is the effective density of states in the conduction band. M_c is the number of band minimums m_e^* the electron effective mass on the semiconductor

The values found on literature for $E_{cs} - E_t$, K_n , M_c and m_e^* (and the obtained value for N_c) are shown on Table 1.1

Table 1.1: Values for the various constants used on equation (1.6)

Parameter	Value
$E_{cs} - E_t$	30 (meV)
K_n	$10^{-13}(m^3s^{-1})$ [24]
N_c	$8,53 \cdot 10^{12}$
M_c	23 [25]
m_e^*	$0,28m_e$ [26][27]

In this way, if an electric field E is induced inside the SnO_2 semiconductor, it is possible to modify its surface state and thus changing its adsorptivity by affecting the number of possible charged chemisorbed states. If the electrical field inside our semiconductor points towards the sample bottom, the offer of electrons is increased, thus promoting the adsorption of reducing adsorbates (donors) and inhibiting the adsorption of oxidizing adsorbates (acceptors). Reversing the electric field produces the opposite effect, promoting the adsorption of reducing adsorbates (donors) and inhibiting the adsorption of oxidizing adsorbates (acceptors). The effect is the same for a p-type semiconductor, noting that in this case a donor would be an oxidizing adsorbate and an acceptor would be a reducing one.

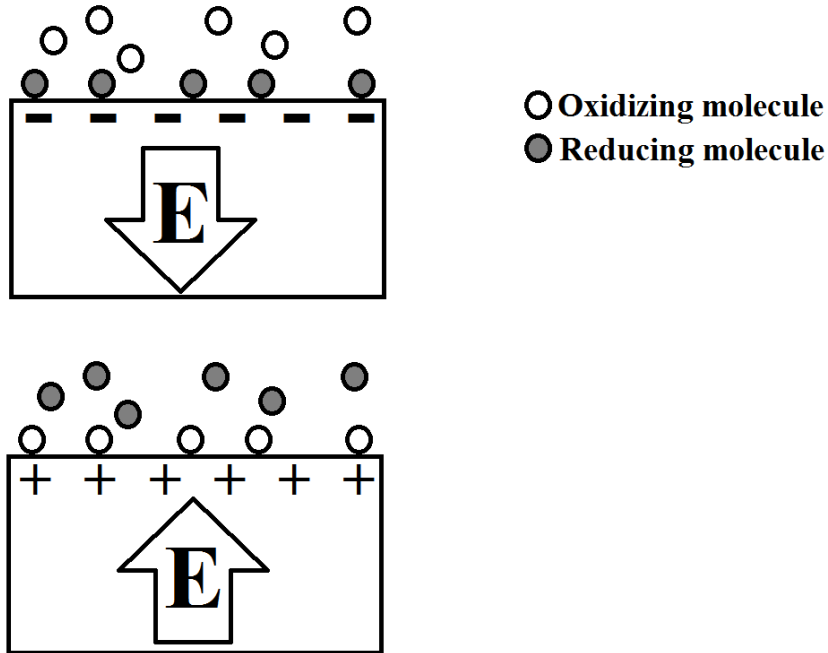


Figure 1.2: Sketch of the electroadsorptive effect for **a** induced electric field E pointing towards the sample bottom and **b** induced electric field E pointing towards the sample surface.

1.4 Other adsorbed species

Organic films can form by the adsorption of molecules from either a liquid solution or vapor phase over a solid surface. Metallic and metal-oxide surfaces adsorb organic molecules in order to reduce the interface free energy between surface and ambient[28]. Some organic films can cover the entire metal-oxide surface, thus having potential uses that range from corrosion resistance[29][30] and thin-film lubrication[31] to surface functionalization[32][33]

Self-assembled monolayers (SAMs for short) are a kind of organic film which can spontaneously organize on a crystalline or semicrystalline structure, forced by both the polycrystalline lattice of the surface and the lateral forces that arise due to the interaction between molecules. The most widely studied SAMs are those generated by the adsorption of alkanethiols on a metal surface such as gold or copper. Alkanethiols have a sulfur-hydrogen “head group” which strongly chemisorbs onto the metallic surface and a concatenated hydrocarbon “tail group” chain which attaches to the head group (see Figure 1.3). The last hydrocarbon of this chain can be chemically altered in order to functionalize the surface, further changing its properties, and its often called “terminal group”. The properties of the SAM are dependent of both the type of head group and the “length” (number of concatenated CH_x molecules) of the tail group [34]. The reported desorption temperatures range from 343 K [35] to 383 K [36] for alkanethiols.

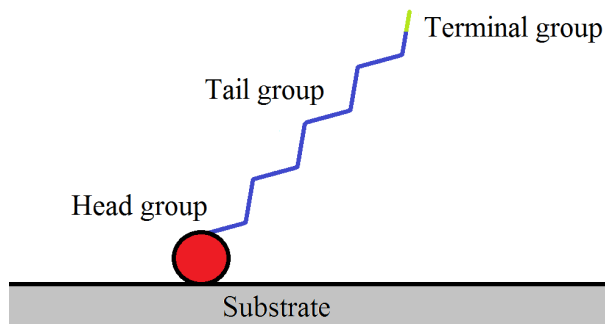


Figure 1.3: Diagram of a thiol on a substrate. The head group (red), tail group (blue) and terminal group (green) are shown.

1.5 Atomic Force Microscopy

The atomic force microscopy (AFM) is one kind of scanning probe microscopy (SPMs). SPMs are designed to measure local properties, such as height, with a probe. In AFM a tip is scanned across a surface at close distance, tracing the surface contour. Inter-atomic, frictional, magnetic and electrostatic forces attract or repel the tip, which is mounted to a flexible cantilever (Figure 1.4). The resulting deflection of the cantilever can, in turn, be used to produce an image of the surface, e.g. by generating lines of equal force. In most AFM applications the cantilever touches the surface during scanning and the feedback signal is derived from the normal force, which is calculated as a function of the flexion of

the cantilever. The cantilever is irradiated by a laser, and its reflection is collected by a photodiode. The position of the reflected laser allows the measurement of the deflection. [37]

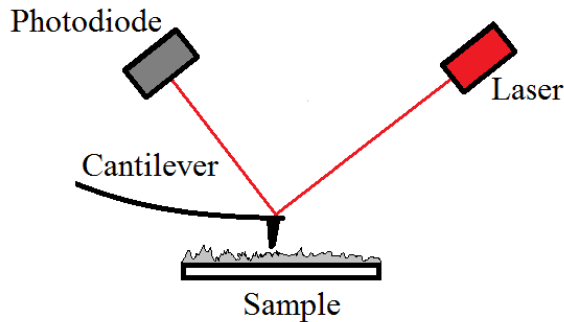


Figure 1.4: Diagram of AFM working principle

1.6 Low Energy Ion Spectroscopy

Low-energy ion scattering (LEIS) or ion scattering spectroscopy (ISS) uses a beam of ionized particles in order to identify the elements at the first atomic layer. These ions are elastically scattered by the surface atoms, and the resulting scattered beam is observed. Each element at the surface produces a peak at different measured kinetic energy (which is caused by the momentum transfer between ion and atom). This transfer is dependant of the relative masses of the involved ion and atom and the incident angle of the ion. This is modelled by the following equation

$$\frac{E_1}{E_0} = \frac{\sqrt{(\cos^2(\theta) + (\frac{M_s}{M_i} - \sin^2(\theta)))}}{1 + \frac{M_s}{M_i}} \quad (1.7)$$

Where E_1 is the energy of the scattered ion, E_0 the energy of the ion beam prior surface-collision, θ is the scattering angle, M_s is the mass of the scattering surface atom and M_i is the mass of the ion. If $M_s < M_i$ there is no back scattering. A diagram of the ion interaction can be seen on Figure 1.5

Here, the surface atoms are represented by a white circle, while the ions are shown as a colored circle. The red arrows symbolize the velocity of the ion before and after its collision with the surface. θ is the scattering angle. The energy E_0 is typically around 1keV or lower. This ensures that ions that penetrate beyond a monolayer nearly always emerge as neutral atoms. Since the detector used for this kind of measurement only detects charged particles, this technique is surface-sensitive. [38]

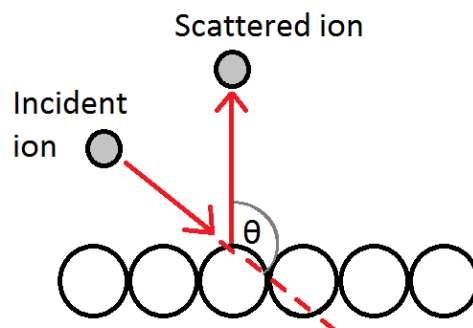


Figure 1.5: Diagram of the geometry used for LEIS.

1.7 X-ray photoelectron spectroscopy (XPS)

Photoelectron spectroscopy utilizes photo-ionization and analysis of the kinetic energy of the emitted photoelectrons to study the composition of the surface of a sample.

When soft monoenergetic X-rays irradiate a sample surface, they interact with the surface atoms, causing electrons to be emitted by the photoelectric effect. They have kinetic energies KE given by:

$$KE = h\nu - BE - \phi_s \quad (1.8)$$

Where $h\nu$ is the energy of the inciding photons, BE the binding energy of the atomic orbital where the electron originates and ϕ_s the spectrometer work function. Figure 1.6 shows the working principle of the XPS.

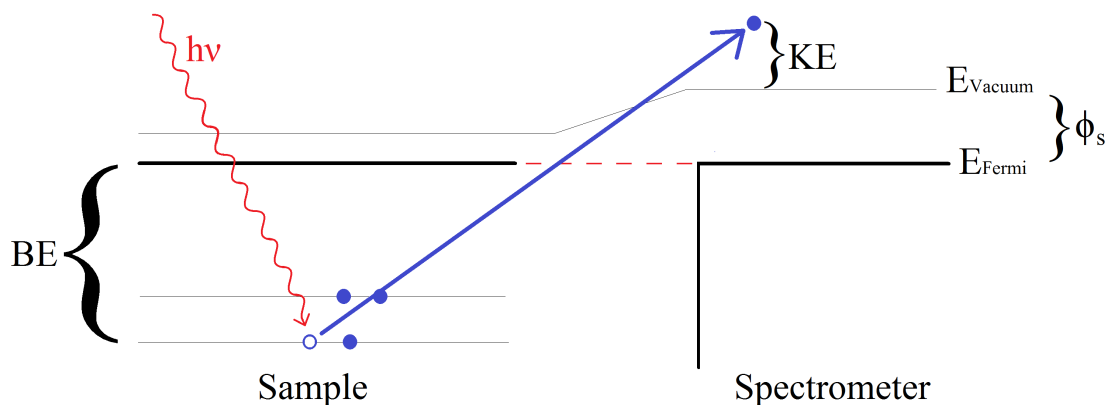


Figure 1.6: Diagram of XPS working principle

Each element has a characteristic binding energy associated to its core levels; this means that each element has a different spectra. By using a known X ray source (The most used

ones are from a Mg $K\alpha$ (1253.6 eV) or Al $K\alpha$ (1486.6 eV) cathode) and by measuring the kinetic energy of the emitted electrons, we can determine their binding energy by using equation (1.1) which allows us to identify the elements at the surface. Variations in the elemental binding energies (chemical shifts) arise from differences in the chemical potential and polarizability of compounds. These shifts can be used to identify the chemical state of the material being analyzed.

While the depth penetration of the X-rays is high (a few micrometers) the mean free path of the photoelectrons is quite small in comparison ($\lambda \leq 10nm$) and most of the detected electrons come from that depth.

1.7.1 Time resolved measurements

In order to obtain the time evolution of the XPS spectra, the “Depth profile” function (included in the operating software of the XPS) was used. This function normally records a spectrum before eroding the sample surface by activating an Ar ion gun by a set amount of time, alternating between gun activation and spectrum recording. By turning off the ion gun, we can easily obtain multiple spectra automatically.

1.8 Mass Spectrometer

The residual gas analyzer operates by ionizing some of the gas molecules present by bombarding them with electrons derived from a heated filament. The ions are then directed toward a voltage mass filter which can successfully separate ions, based out on their mass-to-charge-ratio.

The mass to charge ratio is expressed as M/Q , where M is the atomic mass unit, which is defined as 1/12 of the mass of a single ^{12}C carbon isotope. Q is measured in units of electron charge e^- .

Chapter 2

Experimental setup

In this chapter we describe the implemented experimental setup during the realization of this thesis. Each part is described in detail.

2.1 General description

A special setup is required in order to perform this experiment. It should allow the polarization of a sample under high vacuum conditions, the insertion and quick evacuation of a NO_2/O_2 mixture and sample translation to the XPS measuring zone while maintaining at all times the polarization on the sample. Since no such chamber was available at the start of this thesis, it was built from scratch.

Figure 2.1 shows the schematics of the setup. It consists of a turbomolecular pump assisted by a rotary vane pump and a sampleholder attached to a linear motion magnetic transporter. The sampleholder is provided with two electrical connections which go through a vacuum feedthrough to a DC power source. There is also a gas source, a mass spectrometer and a pressure gauge.

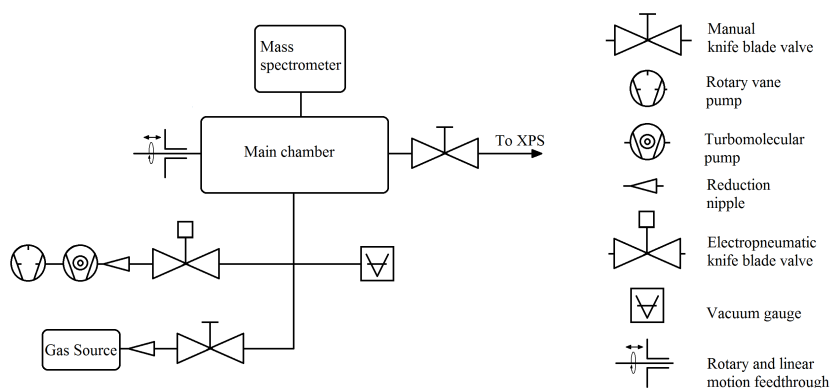


Figure 2.1: Experimental setup schematics

2.1.1 Insertion arm

Figure 2.2 shows a picture of our insertion arm system. It consists of a linear motion magnetic transporter (1) which has been fitted with a MACOR ceramic cylinder with a duraluminum cover(2). The ceramic has six small perforations, two of them with female contacts embedded on them (3). The contacts are connected to the vacuum feedthrough by two 600 mm. long kapton-insulated wires which are coiled around the inner tube of the magnetic transporter (4). The other four holes are left empty, but available for preparing electrical connections in a similar fashion for different possible measurements (e.g measuring the surface conductivity of a sample). Attached at the end of the ceramic piece there is a duralumin holder (5) where the sampleholder (6) can be mounted. The vacuum feedthrough is connected to a DC power supply with a 200 Ω resistance in series. The resistance is there both as protection for the power source, in case there is a shortcut in the sample, and as a reliable way of measuring the current circulating through the circuit.

This system allows for our sample to be moved from the small adsorption chamber to the XPS measurement position, while being able to control the sample polarization at all times.

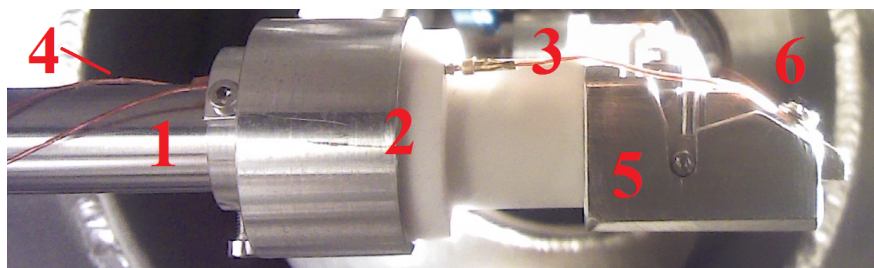


Figure 2.2: Side view of the insertion arm.

2.1.2 Sample holder

The sampleholder is a hollowed duralumin prism, with a MACOR ceramic piece attached to it. It has a fixed angle of 55° with respect to the horizontal in order to maximize the electron count on the XPS. On the ceramic piece, two screws are added for affixing the sample and maintaining the required electrical contacts. Figure 2.3 shows pictures of the sampleholder. Insert **a)** shows a lateral view and insert **b)** presents a frontal view. Both views have a red line showing the scale in millimeters.

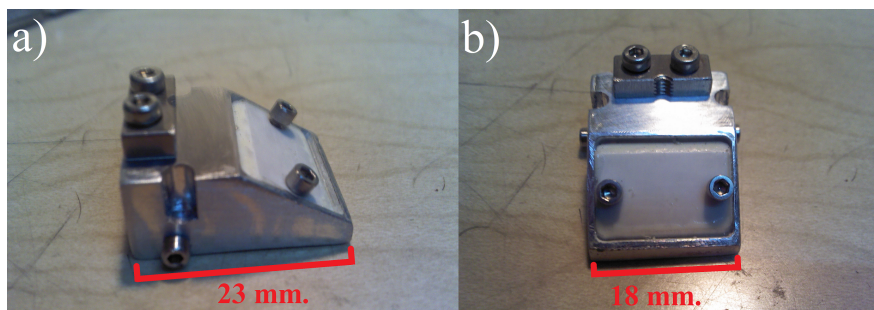
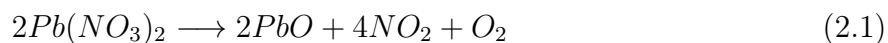


Figure 2.3: Pictures of the sample holder. The red line shows its scale.

2.1.3 Gas Source

In order to produce the desired NO_2/O_2 mixture, a small stainless steel receptacle canister filled with lead nitrate $\text{Pb}(\text{NO}_3)_2$ was used. Lead nitrate decomposes at around $205\text{ }^\circ\text{C}$ following this chemical reaction:



The canister is connected to the adsorption chamber via a knife gate valve. In order to achieve the decomposition temperature, the canister is enveloped by a Nichrome coil which is, in turn, covered by small ceramic beads. These beads act as an electrical insulator for the Nichrome wire. Furthermore, the aforementioned setup is covered by an insulating layer made out of alumina wool and Al sheets.

The Nichrome coil is connected to a variable autotransformer which supplies the electrical power needed for our system to heat via Joule effect. The temperature is controlled by a K-type thermocouple located inside the alumina cylinder, at the surface of the receptacle.

2.1.4 Mass Spectrometer

A Residual Gas Analyzer Stanford Research System ERS model 100 is located in the adsorption chamber. Its repeller grid is 13 mm above the sample surface. This allows us to monitor the different gases inside the chamber with a sensitivity of 10^{-7} Pa, and is used for ensuring that the NO_2/O_2 mixture is flooding the chamber.

2.1.5 Gas atmosphere

The base atmosphere of the adsorption chamber, shortly after baking, was measured using the mass spectrometer in the histogram mode. By running the “analyze” routine on the RGA software controller, signals of hydrogen, carbon dioxide, oxygen and water were found in the chamber. Their relative percentage is shown in Table 2.1.

Table 2.1: Relative percentages of gases in chamber

Element	Relative percentage
Hydrogen	71
Oxygen	0
Nitrogen	11
Carbon Dioxide	4
Water	14

Since the chamber was vented using air, the water relative percentage increases after a few samples are put inside, reaching an equilibrium value around 50 percent. At this point, the pressure inside increases to $P \approx 2 \cdot 10^{-5}$ Pa.

After sample introduction and pumping, the chamber is flooded by the NO_2/O_2 mixture to a total pressure $P_2 \approx 7 \cdot 10^{-4}$ Pa, or a partial pressure of around $P_{\text{NO}_2} \approx 10^{-5}$ Pa. The relative percentages inside are shown on Table 2.2

Table 2.2: Relative percentages of gases in chamber during flooding

Element	Relative percentage
Hydrogen	2
Oxygen	10
Nitrogen	2
Carbon Dioxide	7
Water	39
NO	36
NO ₂	4

The sample is exposed to this atmosphere for 10 minutes before being moved into the XPS chamber. This is equivalent to 4500 L (Langmuir) of NO_2 exposition.

2.2 Sample

The sample is made out of a 3 inches p-type Si wafer substrate with 100 nm of thermal oxide. On top of the oxide, a 100 nm film of SnO_2 has been deposited by Radio Frequency sputtering from a SnO_2 target, followed by annealing in dry synthetic air (400C/100h). These samples were provided by Professor Theodor Doll from Hannover Medical School (MHH) located in Hannover, Germany. The wafer was then cut into 10×10 mm pieces. Finally, a Cu C-shaped contact is evaporated by e-beam evaporation onto the sample as a contact, in order to ensure proper grounding of the surface(Figure 2.4).

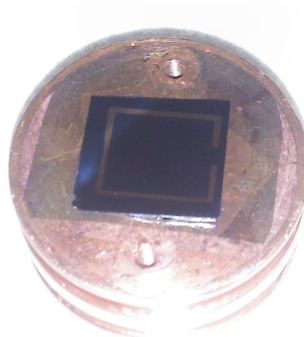


Figure 2.4: Sample, right after contact evaporation

2.2.1 Surface potential measurement

In order to check the conditions under which the C-shaped contact effectively provides an equipotential surface, and to map the potential distribution at the surface, the sample was probed (in ambient conditions) in various places with a metallic probe. A set of copper dots were evaporated by e-beam evaporation on top of some samples (after evaporation of the C-shaped contact) as seen on Figure 2.5. Each dot is 1 mm apart. These dot contacts were used to ensure a proper ohmic contact between the probe tip and the sample. The voltage measurement was made using a Keithley 2100 6 1/2 digit resolution digital multimeter, with an impedance of 10 M Ω .



Figure 2.5: Sample with the point contacts used for the surface potential measurement

2.2.2 Circuit

Various DC potential values were applied to the sample in order to generate an electric field perpendicular to its surface, which is grounded in order to avoid surface charging and subsequent XPS peak shifting. Figure 2.6 shows the schematics.

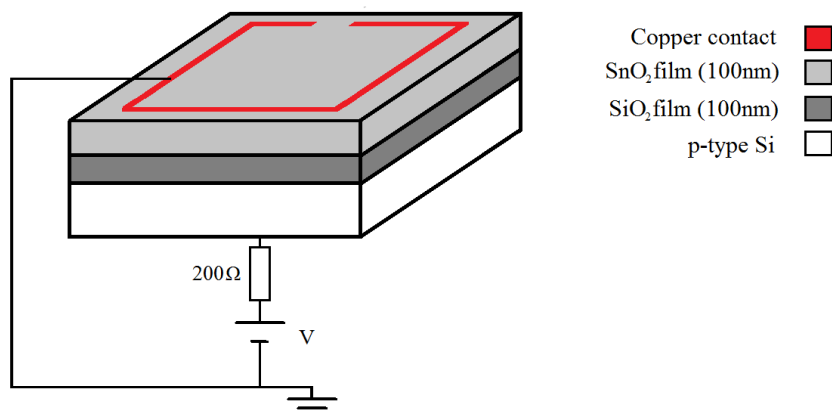


Figure 2.6: Schematics of the circuit used.

2.3 Other experiments

In order to explore new possibilities for the electroadsorptive effect, two different substances were deposited on top of the sample in order to form a molecular monolayer on its surface.

2.3.1 Titanium oxide

A thin TiO film was evaporated on top of the SnO₂ sample by electron beam evaporation. Its thickness (nominally 1 nm) was controlled by a quartz crystal microbalance. Afterwards, the Cu contacts were deposited onto this new sample and a backside polarization voltage was applied to the sample in order to observe if the equipotential condition is conserved. It is worth noticing that the TiO film immediately oxidizes to TiO₂ when exposed to air. A LEIS spectrum was taken in order to ensure total TiO₂ coverage onto the SnO₂ surface. The gas used for LEIS was He⁺ with an energy $E_1 = 0,7$ keV. The idea of this experiment is to check whether the surface equipotential is maintained even if said surface is composed of a few atomic layers of a different material.

2.3.2 Thiols

Dodecanethiol molecules were deposited on top of the samples by immersion on a thiol solution. The solution was made using 1-dodecanethiol (at a concentration of 98%, purchased at Sigma-Aldrich) diluted on 2-propanol until a concentration of 10 mM was achieved. The sample was immersed in this solution by 12 hours at laboratory conditions. Afterwards, and in order to remove any thiol molecule not bound to the sample surface, the sample was thoroughly rinsed with 2-propanol and dried with gaseous nitrogen [39]. Finally, the copper contacts were evaporated on top of the thiolated SnO₂ surface. The contacts were evaporated after the immersion in order to avoid thiols adsorbing on the copper surface.

2.3.3 Topographical characterization

In order to check whether the surface experiments topographical changes during electroadsorption, AFM images were recorder before and after the experiments were made on a set of samples. These images were processed using the software WSXM [40].

Chapter 3

Results

This chapter describes the experimental steps, sample preparation and measurement.

3.1 Preliminary measurements

3.1.1 XPS spectra at $\phi = 0$

Figure 3.1 shows the full XPS spectrum recorded from the tin oxide sample located at the sample holder. The program Multipak was used to identify each signal.

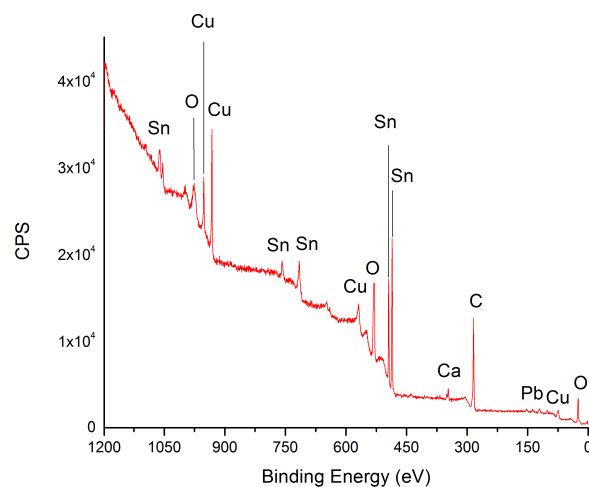


Figure 3.1: Survey spectrum when the sample is not polarized.

As expected, we observe Sn, Cu, C and O. Small traces of Ca are ubiquitous in all our measurements and may be attributed to handling during either sample or contact preparation. The large amount of carbon present in the sample is attributed to the preparation of the back Al contact, a process performed in a vacuum chamber assisted by a diffusion pump. Also, traces of Si and Pb were detected. The presence of Si is attributed to the edge of the sample, while Pb can be present due to lead oxide of the gas source. The Cu signal comes from the C-shaped contact deposited on top of the sample.

High resolution spectra of the Sn 3d, Cu 2p, C 1s and O1s peaks were recorded for comparison, and are shown on Figure 3.2 a,b,c and d respectively.

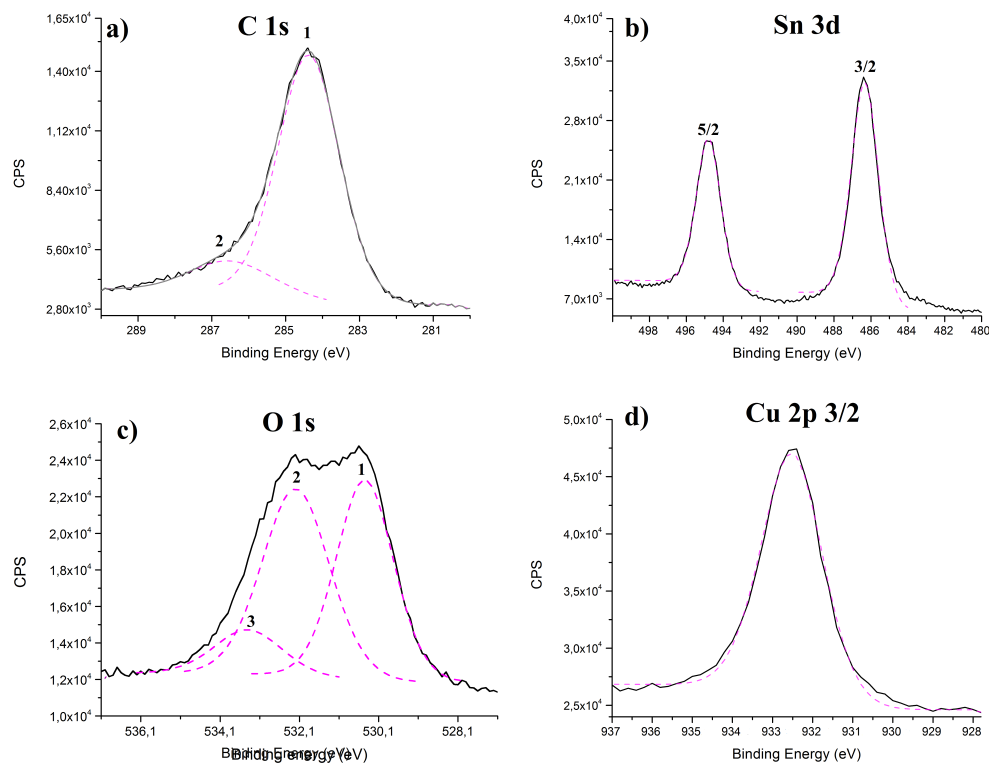


Figure 3.2: High resolution spectra of the non polarized sample.

The raw signal obtained by the XPS is in black, while the Gauss-Lorentz adjustments are in pink. The energy maximum of each curve, their FWHM and the assigned chemical state are shown in Table 3.1

Table 3.1: Peak positions, FWHM and chemical contribution at 0 V

Signal	Position	FWHM	Associated Chemical State
C 1s	284,5	2,0	Carbon
	286,7	2,5	Carbonate
Sn 3d	486,4	1,7	Tin (IV) oxide
	494,9	1,5	Tin (IV) oxide
O 1s	530,4	1,6	Metal oxide
	532	1,8	Carbonate
	533,1	2,0	Water
Cu 2p _{3/2}	932,6	1,7	CuO

The high resolution spectra of C shows that the carbon contamination is in the form of carbon and some carbonates. The tin is completely oxidized and copper is partially oxidized due to air exposition. Water was detected on the sample surface (by observin the O 1s spectrum), which hints that the SnO₂ surface has adsorbed water.

3.1.2 Grounding of the surface

The expected behavior for a MOS device with small Cu contacts on top is that its surface potential is defined by the applied backside potential ϕ with only a small area around the Cu contacts grounded, as depicted in Figure 3.3). As discussed in Section 2, this does not happen if the metal oxide thickness is around 2 Debye lengths. In order to ensure the sample surface is properly grounded, preliminary XPS measurements were recorded with different circuit configurations (shown in Figure 3.4).

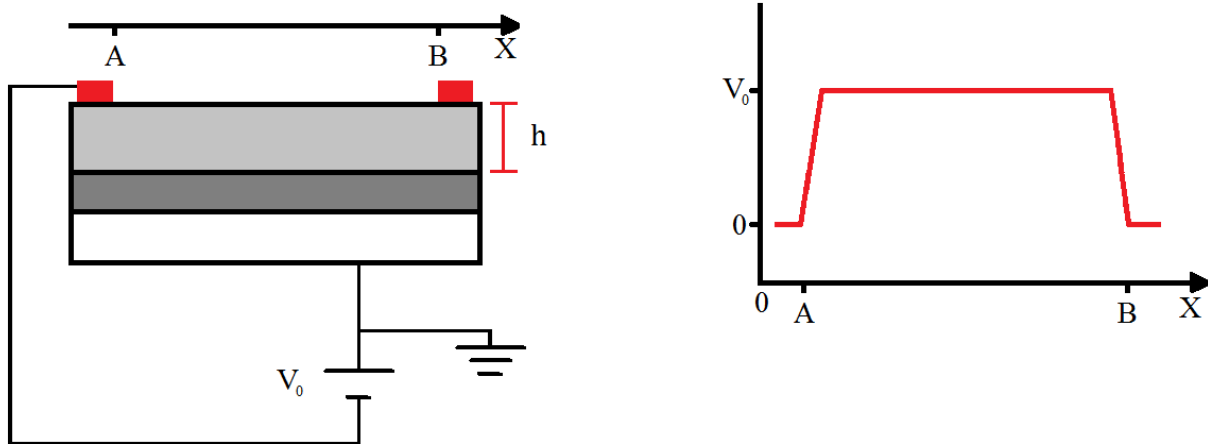


Figure 3.3: Expected behavior for a MOS device with small contacts on top

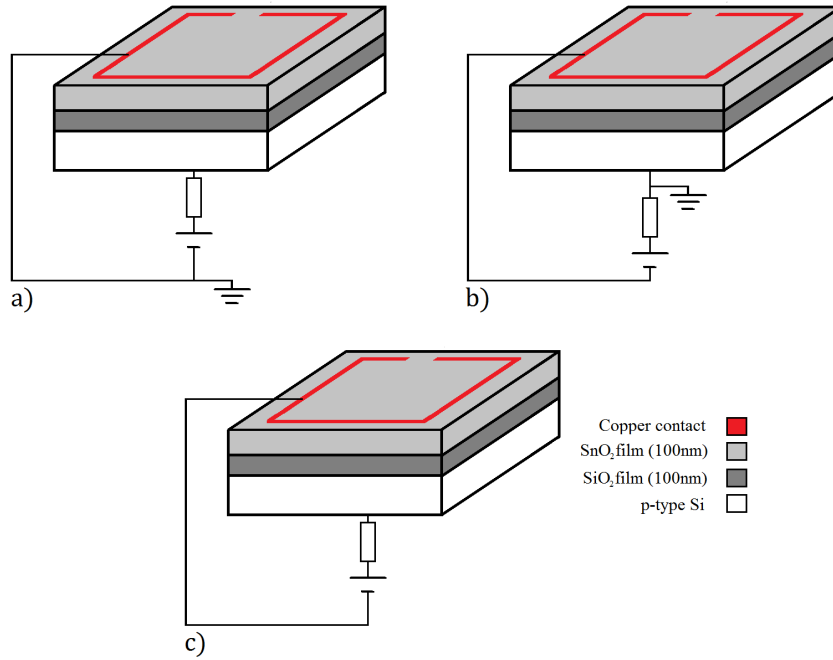


Figure 3.4: Schematics of the different circuits tested

Configuration **a** is grounded at the top of the sample while **b** is grounded at the bottom of the sample. Configuration **c** remains ungrounded (floating).

For the configuration **a**) in Figure 2.6, the Cu signal is not shifted, as observed in Figure 3.5 **c**. The main signal of the C 1s splits in two peaks. The signal that presents the minor shift is labelled “A” while the other is labelled “B” (depicted in Figure 3.5 **a**). The same happens for oxygen, as seen in Figure 3.5 **b**. Signal B is attributed to the charging of the sampleholder, and thus is not considered for further analysis. ΔC_1 was defined as the difference between the carbon peak labelled “A” and the C 1s signal obtained when $\phi = 0$ (labelled “Ref”). A similar calculation was made to obtain and ΔSn_1 . For $\phi > 12V$ and above, there is a peak splitting of the Sn 3d XPS signal, which is also observed on both the C 1s and O 1s spectra. The energy difference between the split signal and the Ref signal have been calculated for C and Sn, and named ΔC_2 and ΔSn_2 respectively. The values for $\Delta Sn_1, \Delta Sn_2, \Delta O_1$ and ΔSn_2 at different ϕ are presented in Table 3.2. While the shifts for the O 1s signal have been studied, since it behaves similarly to the C 1s signal, the values ΔO_1 and ΔO_2 are not reported in Table 3.2. The energy values have been corrected using the Cu $2p_{3/2}$ peak (our grounding contact).

The high resolution spectra of Sn at polarization voltages of $\phi = -15, 0, +15$ (V) can be observed in Figure 3.6. Figure 3.7 depicts the Sn 3d spectrum for $\phi = -12, 0, +12$ (V).

These shifts, for values between -5 V and 5 V are shown in Table 3.2.

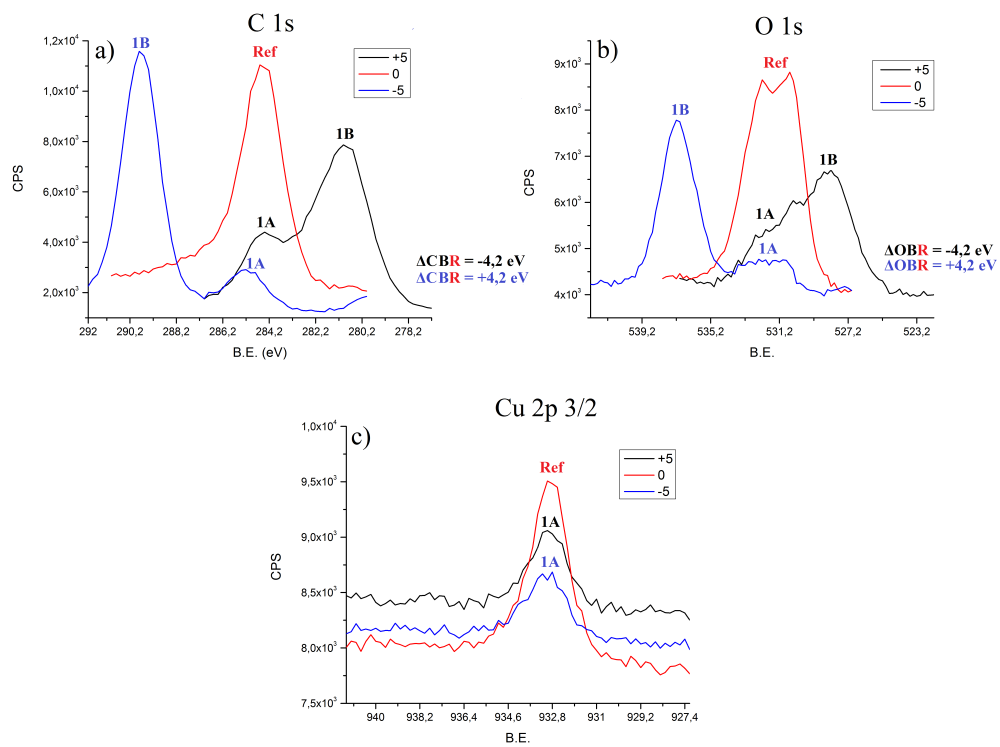


Figure 3.5: XPS spectra of **a** C 1s , **b** O 1s and **c** Cu 2p_{3/2} at different polarization ϕ values.

Table 3.2: Peak shift as function of the polarization voltage ϕ

ϕ (V)	ΔS_{n_1} (eV)	ΔS_{n_2} (eV)	ΔC_1 (eV)	ΔC_2 (eV)
15	-0,6	-3,3	-0,6	-3,2
14	-0,6	-2,8	-0,6	-2,8
13	-0,6	-2,2	-0,6	-2,2
12	-0,6	-1,8	-0,6	-1,8
11	-0,2	–	-0,2	–
10	-0,2	–	-0,1	–
9	-0,2	–	-0,3	–
8	-0,1	–	-0,1	–
7	-0,2	–	-0,2	–
5	-0,1	–	-0,2	–
0	–	–	–	–
-5	0,1	–	-0,1	–
-7	0,1	–	0,1	–
-8	0,2	–	0,2	–
-9	0,2	–	0,2	–
-10	0,4	–	0,4	–
-11	0,5	–	0,5	–
-12	0,5	–	0,5	–
-13	0,5	–	0,5	–
-14	0,5	–	0,5	–
-15	0,5	–	0,5	–

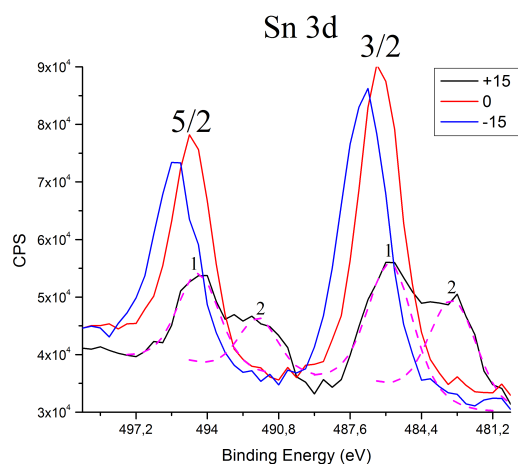


Figure 3.6: Sn 3d spectra at -15, 0 and +15 V. The pink dashed line corresponds to the Gauss-Lorentz curve used for adjustment.

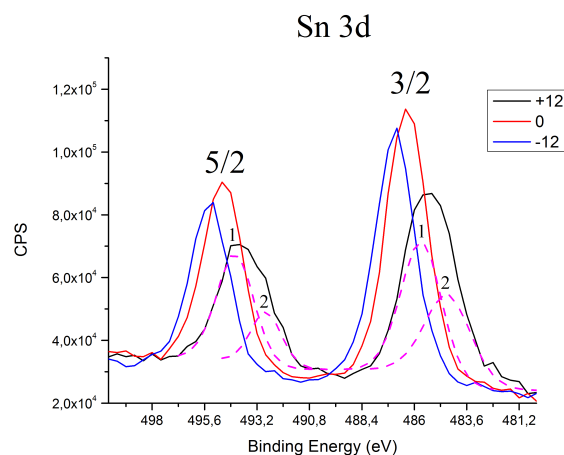


Figure 3.7: Sn 3d spectra at -12, 0 and +12V. The pink dashed line corresponds to the Gauss-Lorentz curve used for adjustment.

3.1.3 Verification of surface contaminants

Due to the relatively high signal of carbon observed on the XPS spectra, and in order to make sure that the SnO_2 sample is not covered by a layer of carbon or another contaminant, a LEIS spectrum was recorded using ^3He ions with a primary energy of $E_0 = 0.7$ keV. The spectrum is shown in Figure 3.8. The peaks were identified using equation (1.7)

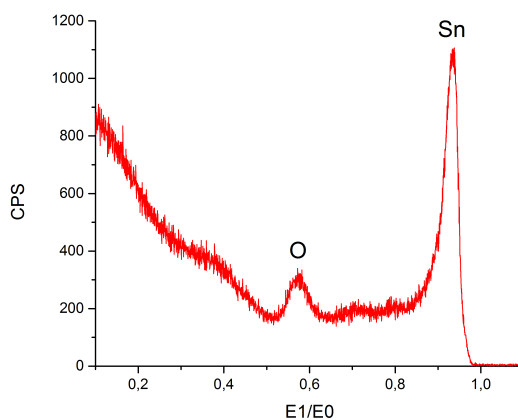


Figure 3.8: LEIS spectra of a sample with evaporated contacts. The associated element to each peak is labelled on top.

The peaks correspond to oxygen and tin, which are attributed to the tin oxide on top of the sample. The tin signal becomes larger with time, and this is believed to be due to

desorption of H atoms (which cannot be observed via XPS) from the sample surface. Since a Sn signal is detected, the sample is not completely covered by contaminants and adsorption may happen onto the SnO₂ surface.

In order to remove all surface contaminants, the sample was eroded by using an Ar ion gun with an energy of 2 keV with a primary ion current of 1 μ m. The sample surface was bombarded by the ion beam for 10 minutes, which amounts to less than 5 nm of surface erosion. However, after the erosion process was performed, the surface equipotential could not be maintained even for $\phi = 5V$. Considering this, the removal of surface contaminants by surface erosion was discarded.

3.1.4 Direct measurement of the surface potential

The samples with dots of copper as contacts on top were used to directly measure the potential distribution on the sample surface as function of ϕ . The representative values obtained are presented as a series of contour lines graphics, shown on Figures 3.9, 3.10, 3.11 and 3.12. The dotted pink line represents the copper contact on top of the sample. The red circles represent a dot-contact, and the numbers below them are the voltage values measured at their positions (in mV).

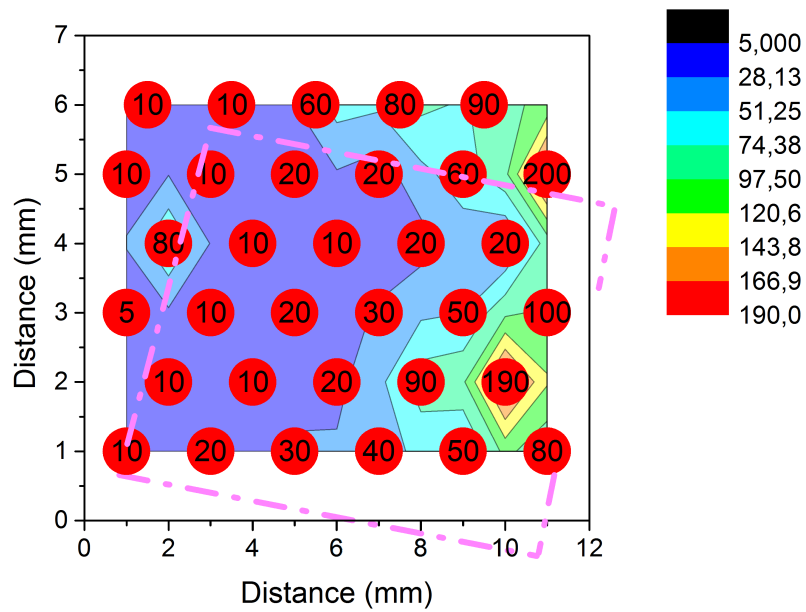
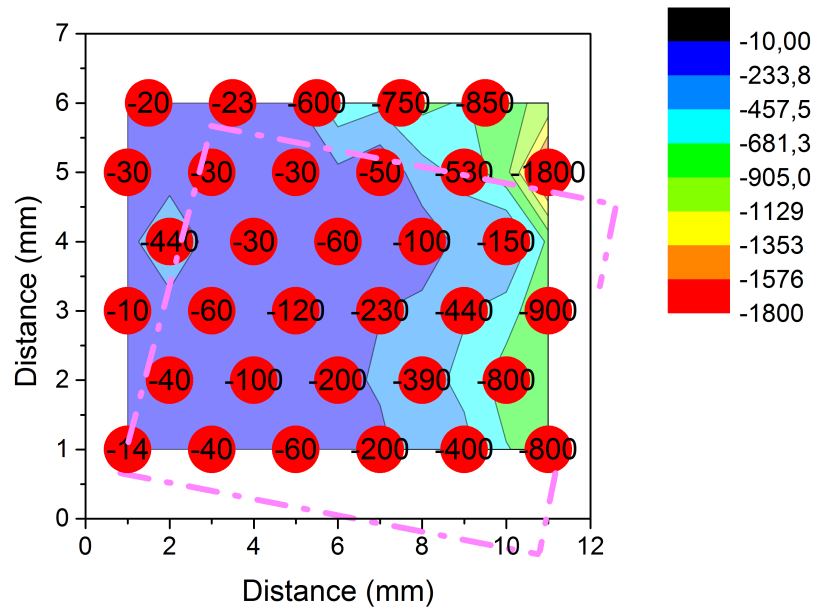


Figure 3.9: Contour line plot for $\phi = -5$ (top) and $\phi = +5$ (bottom).

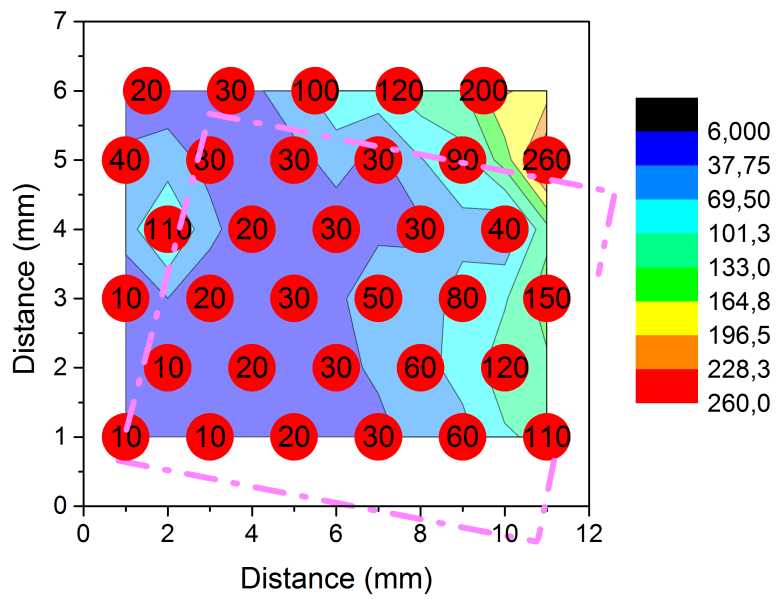
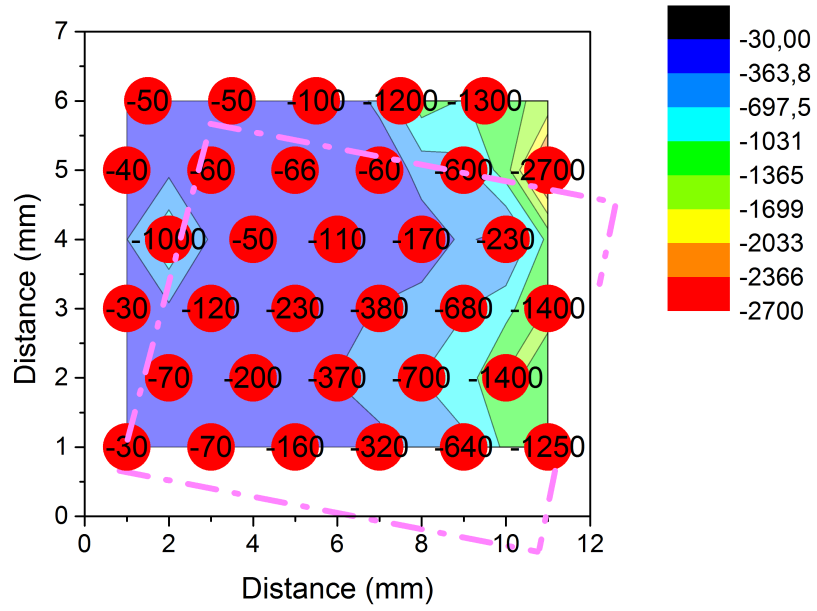


Figure 3.10: Contour line plot for $\phi = -9$ (top) and $\phi = +9$ (bottom).

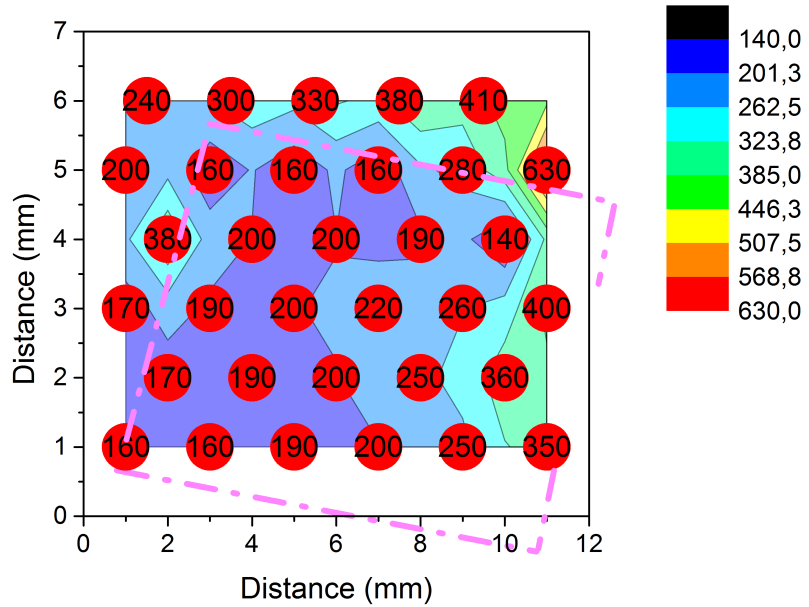
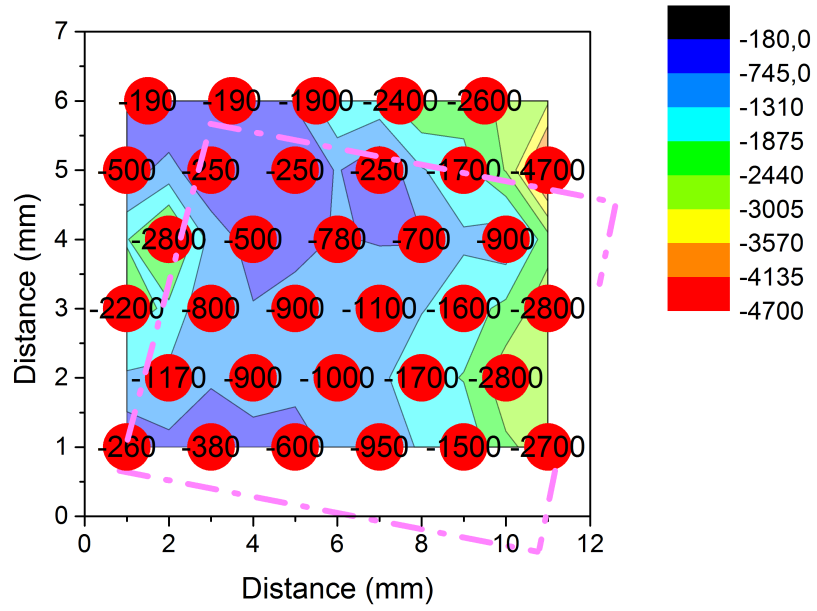


Figure 3.12: Contour line plot for $\phi = -15$ (top) and $\phi = +15$ (bottom).

The behavior of the surface potential depends on whether the applied backside voltage is positive or negative: At positive voltages ($\phi > 0$) the surface is relatively equipotential inside the C-shaped contact, even at +15 V. However, for $\phi < 0$ this condition is hardly maintained: For $\phi = -15V$ the voltage difference measured in some dots is below -2800 mV. In both cases, however, it is noted that the potential is higher when nearing the small opening in the C-contact, as expected. It is worth noting that, for negative ϕ , the sample surface has a higher voltage difference in the half that's nearer the open part of the C.

3.2 Exposition to the NO₂/O₂ gas mixture.

Subsequently, a set of samples were exposed to the aforementioned gas mixture during 10 minutes and various XPS spectra were recorded under three different experimental conditions:

- Subsection **3.2.1** shows the results obtained when the sample was never polarized
- In subsection **3.2.2** the sample was exposed to the gas while its backside remains polarized (using the circuit depicted in Figure 3.4 **a**) at various ϕ values and afterwards moved to the XPS main chamber. Then, the polarization voltage ϕ was turned off and spectra were recorded.
- Finally, in subsection **3.2.3** the sample was polarized at different ϕ values while exposed to the gas, but the polarization was never turned off.

In all three cases, the time required to remove the gas from the adsorption chamber, transferring the sample to the main XPS chamber and starting to record the spectra is less than 40 seconds. The time t used in all graphs refers to the one measured immediately after the recording process started. In order to obtain more counts per second (since the N 1s signal was quite low) the XPS spectra were recorded using a pass energy of $E_{p1} = 89,45$ eV, instead of the commonly used value of $E_{p2} = 44,75$ eV. Victor Fuenzalida [41] used Au in order to calibrate the data deformation due to a different pass energy, and estimated that the FWHM of the peaks observed with E_{p1} is approximately 1.5 eV bigger than the one measured with E_{p2} , which accounts for the rather broad (FWHM = 2,5 eV) peaks obtained.

The interpretation of the N 1s XPS spectra components has been discussed in the literature. The summary of the reported peaks are presented in Table 3.3.

It is worthwhile noticing that the sampleholder was warm to the touch after around 1 minute after XPS measurements. As this was detected even when no voltage was applied to the sample, this cannot be attributed to Joule effect, but to thermal radiation from the filament of the x-ray source.

Table 3.3: Binding energy (eV) of the N 1s peaks.

Peak id.	Binding energy (eV) and species identification						
Ref	[42]	[43]	[44]	[45]	[46]	[47]	[48]
N1	1	398,1		398,1	398,2	398 - 398,3	398
	-	Elemental nitrogen	Elemental nitrogen	Elemental nitrogen	C - N	C - N	Fe - N
-	397,5 - 401,4	398 - 400	401,5	401,5	400,1 - 400,7	398,9 - 400	399,5
	NO	Organic matrix	N ₂ O	N ₂ O	C - N	C - N	Fe - N
N2	402,3 - 405,1	404 - 405	403,5	403,5	-	-	405,2
	NO ₂	NO ₂	NO	NO	-	-	NO
N3	406,3 - 408,1	406 - 408	-	-	-	-	-
	NO ₃	NO ₃	-	-	-	-	-
Comments	NO ₂ on γ -Al ₂ O ₃ and α -Fe ₂ O ₃		NO on Au	NO on Au	CNx films	CN films	NO on hematin

3.2.1 Sample never polarized

Figure 3.13 shows a typical N 1s spectra obtained at different times while the sample was never polarized. The larger signal, centered around 399 eV, was labelled “N1”. Normally, a signal as broad as N1 requires at least two curves in order to obtain a good fit. However, since the signal is too noisy it was decided to only use one, centered at 399 eV, even if it has a rather large FWHM of around 2,8 eV. A second noticeable signal is observed at around 407,0 eV which is labelled “N3”. Finally, since the adjustment using only 2 curves is unable to properly cover the zone around 402-404 eV, an extra curve centered at 404,0 eV (“N2”) was added. Since [42] is based on the adsorption on a metal oxide surface, the N2 and N3 were identified as adsorbed NO₃ and NO₂. N1 was identified as elemental nitrogen [43].

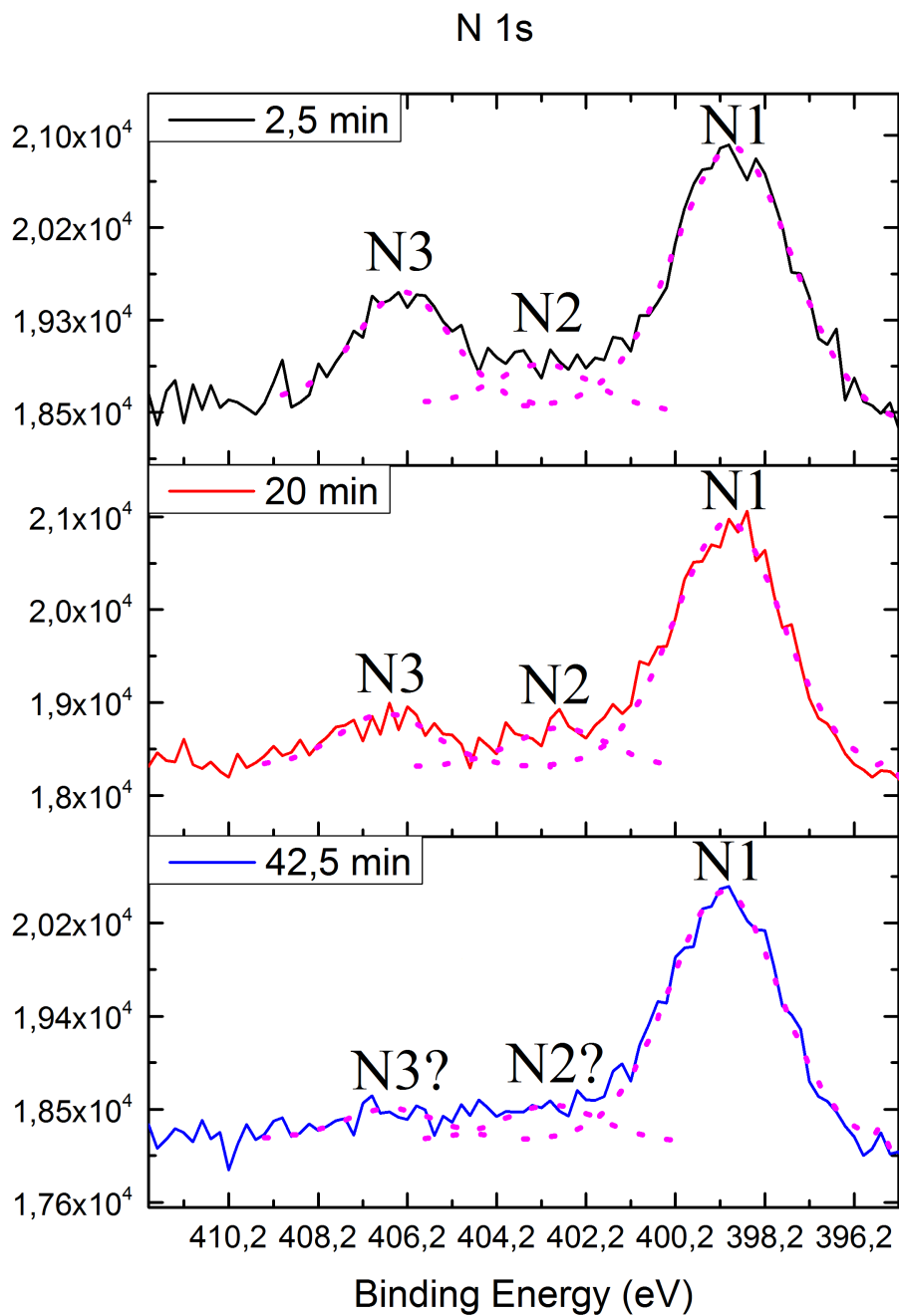


Figure 3.13: N 1s XPS spectra recorded at **a** $t = 2,5$ min, **b** $t = 20$ min and **c** $t = 42,5$ min after the measurement started.

Figure 3.14 depicts the area of the $\text{NO}_2 + \text{NO}_3$ signal as a function of time. An exponential fit was performed on these data, according to Equation (1.4). The data dispersion does not justify using Equation (1.6)

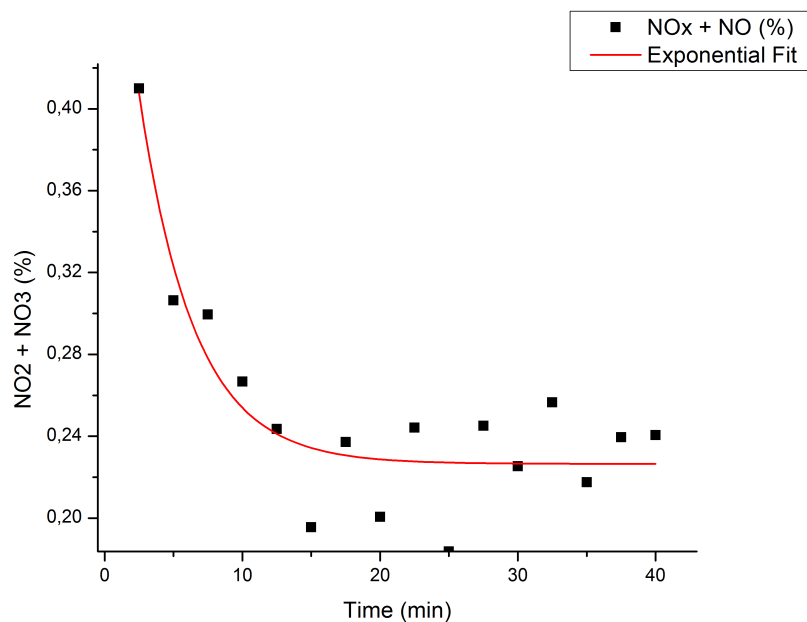


Figure 3.14: Mean curve obtained for $\text{NO}_2 + \text{NO}_3$ concentration onto the SnO_2 surface as function of time. The exponential fit is shown as a red line

Table 3.4 shows the fitting parameters, as well as $\tau = \frac{5}{R_0}$, the estimate of the total desorption time.

Table 3.4: Fitted values for the exponential function parameters. The function used was $f(t) = y_0 + A \exp(-R_0 t)$

y_0	A	R_0	R^2	τ (min)
0.22 ± 0.07	0.34 ± 0.08	0.25 ± 0.06	0.81	20

3.2.2 Sample polarized only during gas exposition

The sample was exposed to the gas mixture for 10 minutes while its back was polarized at potentials $\phi = \{0, \pm 5, \pm 6, \pm 7, \pm 8, \pm 9, \pm 10, \pm 11, \pm 12, \pm 13, \pm 14, \pm 15\}$ V. Immediately after transference to the XPS main chamber the potential was turned off. This was done in order to observe whether the applied potential on the sample has lasting effects on it.

Figure 3.15 shows the N 1s spectra when the sample was initially polarized at $\phi = -15$ and 15 V.

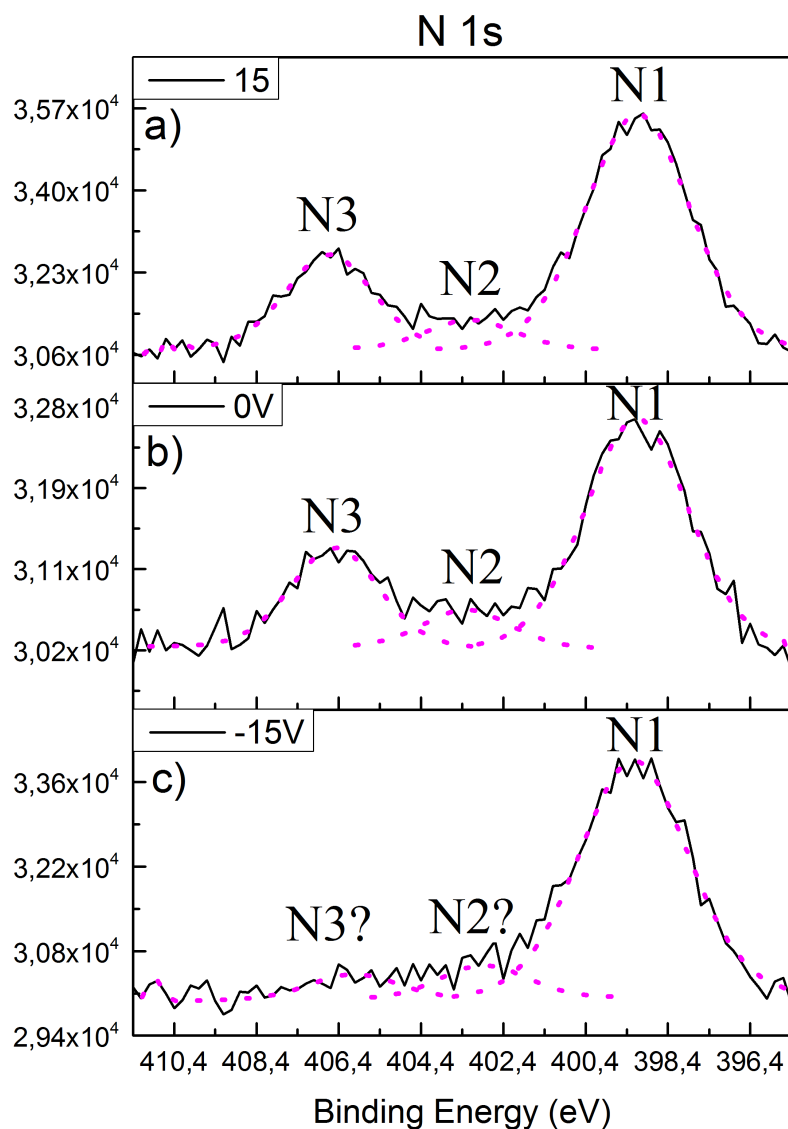


Figure 3.15: N 1s XPS spectra recorded after exposition to the gas mixture while polarized at a) $\phi = +15$ V, b) $\phi = 0$ V and c) $\phi = -15$ V.

We observe a heightened $\text{NO}_2 + \text{NO}_3$ ($\text{N}_2 + \text{N}_3$) concentration (compared to the N (N_1) concentration) at positive back polarization as compared with the case of no polarization.

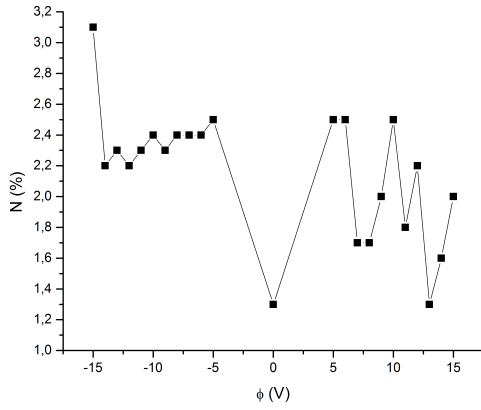


Figure 3.16: N percentage as a function of initial polarization ϕ .

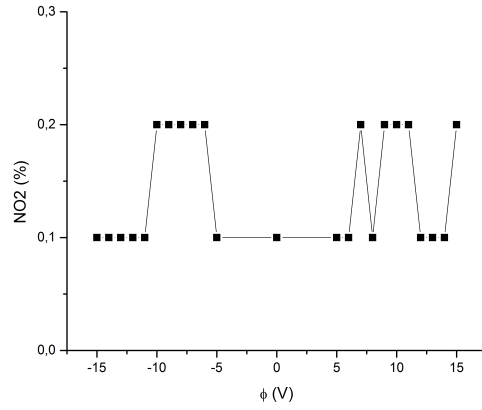


Figure 3.17: NO_2 percentage as a function of initial polarization ϕ .

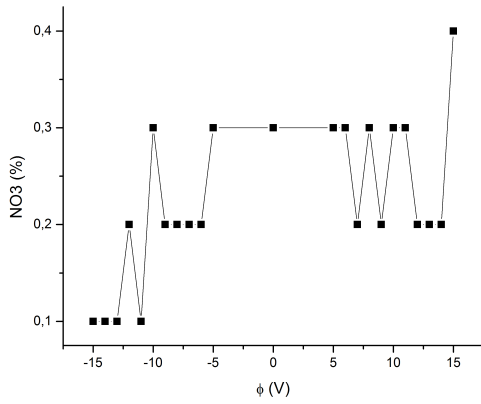


Figure 3.18: NO_3 percentage as a function of initial polarization ϕ .

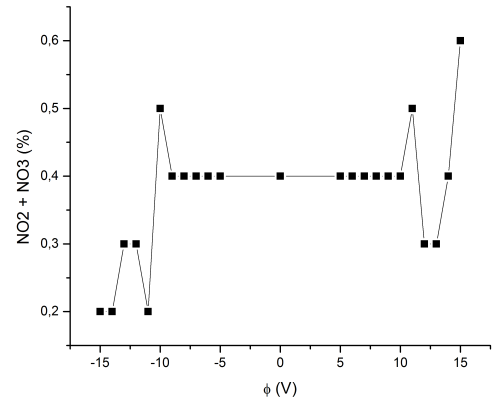


Figure 3.19: $\text{NO}_2 + \text{NO}_3$ percentage as a function of initial polarization ϕ .

Table 3.5 shows the relative percentage of the amount of N , NO_2 and NO_3 species at the surface as function of the initial polarization. Figures 3.16, 3.17, 3.18 show these values, while Figure 3.19 depicts $\text{NO}_2 + \text{NO}_3$ as function of ϕ .

Table 3.5: N 1s, NO₂ and NO₃ relative % present on the sample at t=2.5 min as function of V and the current through the sample

ϕ (V)	N (%)	NO ₂ (%)	NO ₃ (%)	$\sum(NO_2 + NO_3)$ (%)
-15	3,1	0,1	0,1	0,2
-14	2,2	0,1	0,1	0,2
-13	2,3	0,1	0,1	0,3
-12	2,2	0,1	0,2	0,3
-11	2,3	0,1	0,1	0,2
-10	2,4	0,2	0,2	0,5
-9	2,3	0,2	0,2	0,4
-8	2,4	0,1	0,3	0,4
-7	2,4	0,2	0,2	0,4
-6	2,4	0,1	0,2	0,4
-5	2,5	0,1	0,3	0,4
0	1,3	0,1	0,3	0,4
5	2,5	0,1	0,3	0,4
6	2,5	0,1	0,3	0,4
7	1,7	0,2	0,2	0,4
8	1,7	0,1	0,3	0,4
9	2	0,2	0,2	0,4
10	2,5	0,2	0,3	0,4
11	1,8	0,2	0,3	0,5
12	2,2	0,1	0,2	0,3
13	1,3	0,1	0,2	0,3
14	1,6	0,1	0,2	0,4
15	2	0,2	0,4	0,6

The application of a back polarization affects the amount of both NO₂ and NO₃ at the surface. The sum of both species increases if ϕ is positive and decreases if its negative. This effect is barely noticeable for polarization magnitudes of less than 5 V. Two exceptions to this behavior were observed, at $\phi = -10$ V and $\phi = +12$ V using 4 different samples, which evidences that these points are not due to a measurement artifact.

For the elemental N species there is an increased concentration of NO species at the surface when the sample is polarized, regardless of the sign of the polarization.

3.2.3 Sample permanently polarized

XPS spectra were recorded while maintaining the sample polarization during the measurements. Figure 3.20 shows the typical graphs obtained at $\phi = \{-15, -8, +8, +15\}$. $\phi = \pm 5$ was discarded because it showed no noticeable impact on adsorption.

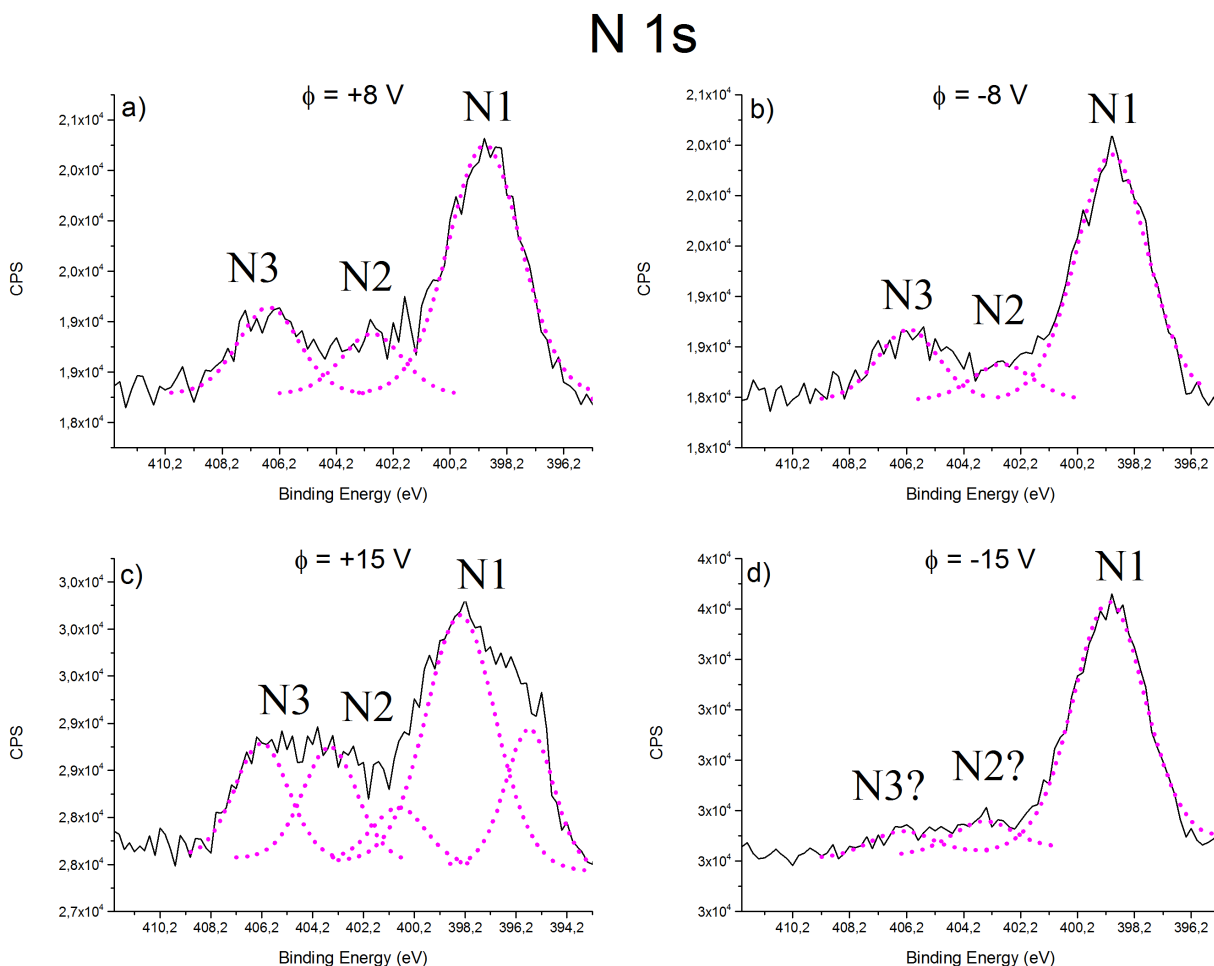


Figure 3.20: N 1s XPS spectra recorded after exposition to the gas mixture while maintaining ϕ at **a)** +8 V, **b)** -8 V, **c)** +15 V, **d)** -15 V.

The application of $\phi = 15$ V splits the NO_3 signal as seen in Figure 3.20. Due to the similarity in the energy difference between this peak splitting (3.3 eV at +15V) and the one observed in the Sn 3d spectrum, it is concluded that this split is produced by a non-equipotential surface, as previously discussed on subsection 3.1.2.

Figure 3.21 show the different relative areas of the adsorbed N species at the representative values of $\phi = \{0, \pm 8, \pm 10, \pm 12, \pm 15\}$ V. The respective exponential fit is shown as a colored line.

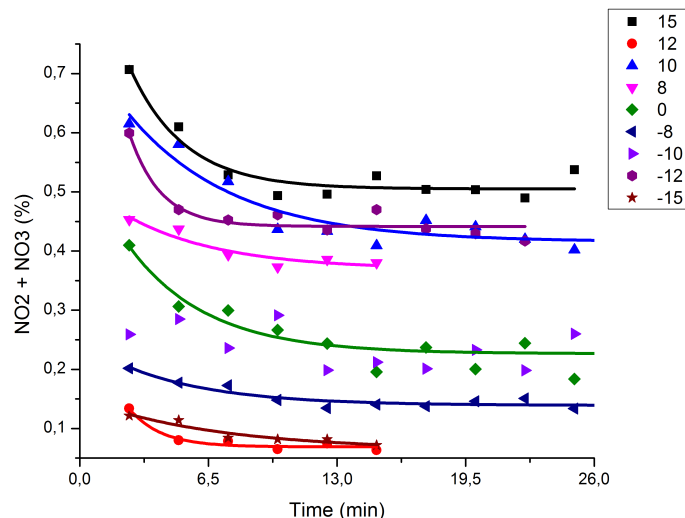


Figure 3.21: $\text{NO}_2 + \text{NO}_3$ relative area as function of time at $\phi = \{\pm 8, +10, \pm 12 \text{ and } \pm 15\}$. The colored line shows the respective exponential fit.

Table 3.6 shows the fitting the parameters obtained as function of ϕ , as well as the characteristic time τ .

Table 3.6: Values of the fitting parameters. The function used was $f(t) = y_0 + Ae^{-R_0 t}$.

V (V)	y_0	A	R_0	R^2	τ (min)
15	0.5 ± 0.1	0.5 ± 0.1	0.4 ± 0.1	0.91	13
12	0.07 ± 0.01	0.3 ± 0.2	0.6 ± 0.2	0.93	8
10	0.4 ± 0.1	0.3 ± 0.1	0.2 ± 0.05	0.88	25
8	0.4 ± 0.1	0.1 ± 0.1	0.2 ± 0.1	0.83	25
-8	0.2 ± 0.1	0.1 ± 0.05	0.2 ± 0.05	0.83	23
-10	***	***	***	***	***
-12	0.4 ± 0.01	0.8 ± 0.4	0.6 ± 0.2	0.88	8.3
-15	0.1 ± 0.02	0.1 ± 0.01	0.2 ± 0.05	0.86	25

Since it was not possible to properly fit the values measured at $\phi = -10V$ (one of the singular points observed in subsection (3.2.2)), they were not added in Table 3.6. At higher polarization, the parameter R_0 increases.

This numerical analysis was performed using data with a higher amount of significant figures than the one used for the analysis in subsection 3.2.2. If the same amount were to be used, the data would not be fit neither by an exponential nor equation (1.6).

3.3 Additional experiments

Two additional experiments were performed in order to test possible new applications for the electroadsorptive effect. First, a thiol layer was formed via solution immersion onto the SnO₂ surface in order to see whether the adsorbed thiolates could be electrodesorbed by this method. The second experiment was to evaporate a thin TiO₂ layer onto the SnO₂ surface in order to see if the equipotential condition could be maintained in the TiO₂.

3.3.1 Thiols on the SnO₂ surface

The thiolated sample with Cu-contacts evaporated on top (as described in subsection 2.2) was introduced into the adsorption chamber. The XPS spectrum recorded is shown in Figure 3.22 1). Afterwards, a +15 V potential was applied to the sample backside for two hours, and a second spectrum was recorded after the potential was turned off (shown in Figure 3.22 2). Finally, a -15 V backside potential was applied to the sample backside for 2 hours, and the third spectrum was recorded (once again, after the potential was turned off). as shown in Figure 3.22 3.

The S 2p spectra have a doublet due to the spin-orbit splitting. This degeneracy is observed as a doublet in the XPS spectrum separated by a fixed energy (1.2 eV in the case of S)[43] and a fixed area ratio, which is based on the degeneracy of each spin state. For the 2p spectra, the area ratio 2p_{1/2}:2p_{3/2} is 1:2 (which corresponds to an electron multiplicity of 2 in the 2p_{1/2} and an electron multiplicity of 4 in the 2p_{3/2}).

Four Gauss-Lorenz adjustment curves (labelled as S1 to S4) were used to fit the experimental curves. In order to account for the previously described spin-orbit splitting, each peak was fitted with its respective doublet (labelled S1A to S4A), with a fixed area of half the area of the 2p_{3/2} signal and centered at an energy maximum which is 1.2 eV shifted respect to the 2p_{3/2} peak. The raw data is shown in black, while the gauss-lorenz adjustment curves are in blue (S1), green (S2), purple (S3) and red (S4). The envelope is shown as a light brown curve.

Table 3.7 shows the maxima of the Gauss-Lorenz adjustment curves (labelled S1 to S4) for all three spectra, the relative percentage of each curve and their interpretation as found in the literature. Its position was corrected using the C 1s peak at 284.5 eV. Satellite signals were removed.

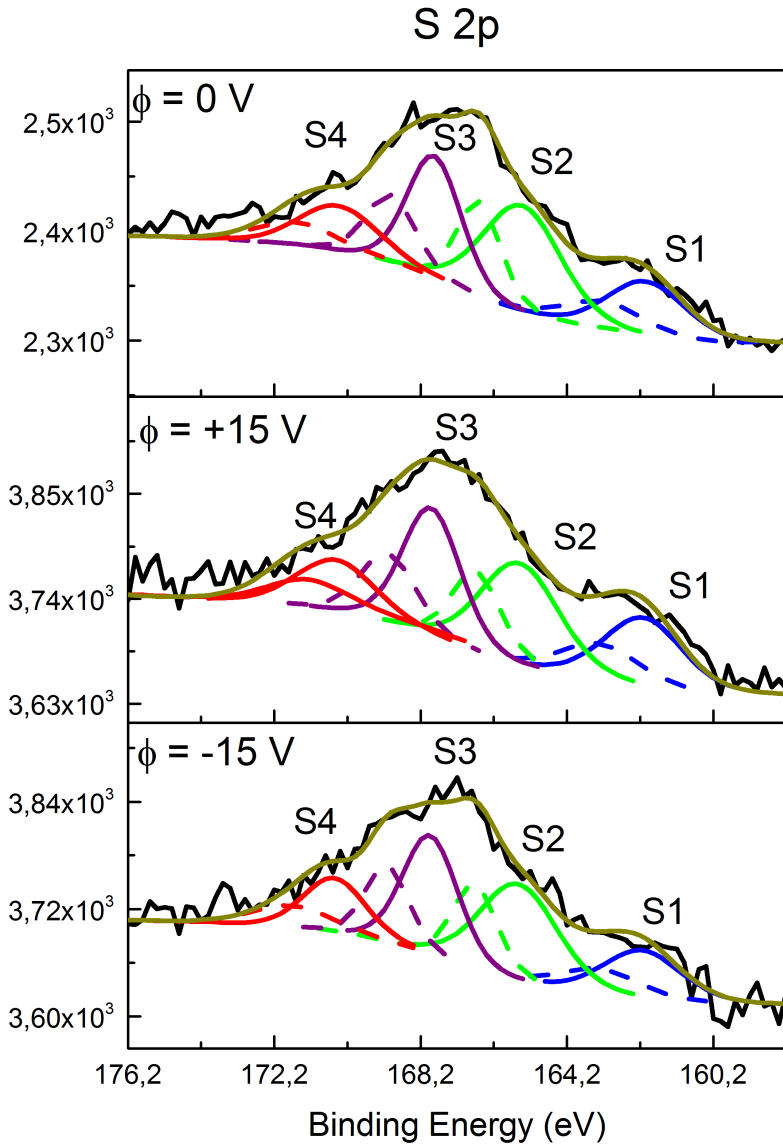


Figure 3.22: XPS high-resolution spectra of the S signal on the sample right after preparation, after a +15 V potential was applied to the sample backside and after a -15V potential was applied to the sample backside.

Table 3.7: Binding energy for each Gauss-Lorentz adjustment curve, its relative percentage compared to the whole S signal and its interpretation as found in the literature

Peak id (energy maxima)	Relative % (fresh sample)	Relative % (After +15 V)	Relative % (After -15V)	Species Identification [ref]
S1 (162,1 eV)	16	16	15	Thiolate [49]
S2 (165,5 eV)	30	30	31	Unbound S [50]
S3 (167,9 eV)	18	19	19	Sulfonate species [49]
S4 (170,5 eV)	36	35	36	Sulfone species [51]

As shown in the table, the peak corresponding to the S1 signal is interpreted as the S-Sn bond of a strongly chemisorbed dodecanethiol molecule, which amount to 15% of the total signal. The signal labelled S2 corresponds to unbound S atoms while S3 and S4 correspond to different types of oxidized sulfur. There are no observed differences induced by the application of $\phi = \pm 15\text{V}$ at the back electrode, so it is concluded that there is no electrodesorption of dodecanethiols at these conditions

3.3.2 Titanium dioxide film on the SnO₂ surface

Figure 3.23 shows the LEIS spectrum recorded from the TiO₂-coated sample, at a scattering angle of approximately 125°. Each peak is labelled with its associated element, which were identified using equation (1.7). The spectrum was recorded using ³He⁺ ions at $E_1 = 0,7\text{ keV}$

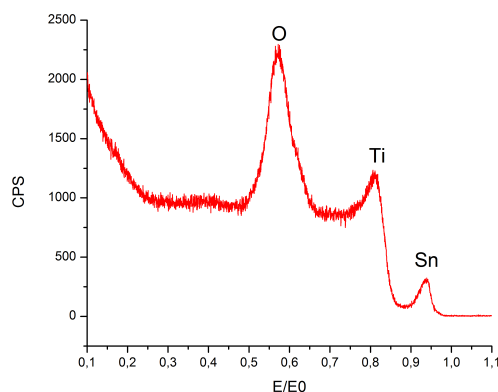


Figure 3.23: LEIS spectra of a sample with a 1 nm Ti film on top.

The spectra shows titanium, oxygen and tin, but no carbon signal is resolved. Since Sn is shown on the spectra, the sample is not completely covered by TiO₂. Consequently, no electroadsorptive effect studies were made since both elements could interact simultaneously with the gas. High resolution XPS spectra of the sample were recorded at $\phi = +15, 0$ and

-15 V, and are shown on Figure 3.24, while the maximum of each peak can be seen in Table 3.8

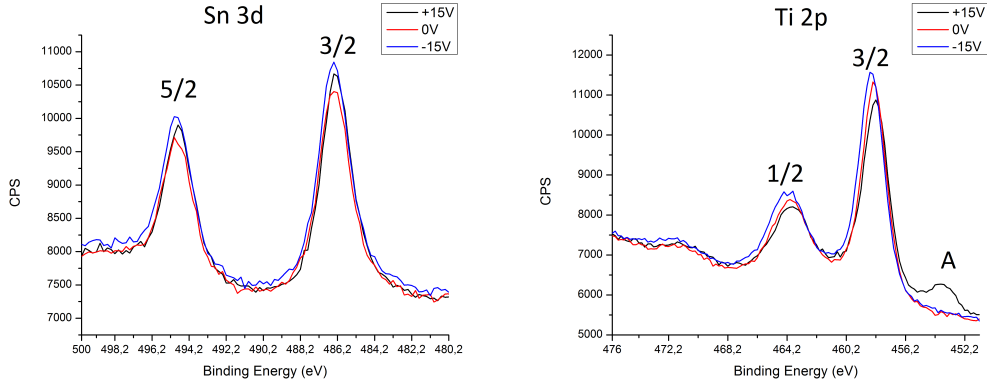


Figure 3.24: XPS spectra of the TiO_2 coated sample at $\phi = +15$ (red), 0(black) and -15 V(blue)

Table 3.8: Ti and Sn peak positions

ϕ (V)	Ti 2p _{1/2} (eV)	Ti 2p _{3/2} (eV)	Ti 2p A	Sn 3d _{5/2} (eV)	Sn 3d _{3/2} (eV)
+15	463,7	458,2	453,8	486,3	494,8
0	463,8	458,3	–	486,4	494,9
-15	464,0	458,5	–	486,5	495,0

A shift of 0.1 eV is observed in the Sn 3d signal when both $\phi = +15$ and $\phi = -15$ are applied. The shift is positive for $\phi = -15V$, and negative for $\phi = +15V$, which is similar for the Ti 2p signal. Since $\Delta E = 0,1$ eV is within experimental error, the TiO_2 layer does not disrupt the equipotential layer on the sample surface. However, when $\phi = +15$ a small peak appears at 453,8 eV (labelled Ti 2pA). This peak is not observed at no polarization, neither at $\phi = -15V$ and its attributed to partial surface charging.

3.3.3 Topographical characterization

Figure 3.25 show a 500×500 nm topographical image of a SnO_2 sample before and after it was exposed to our gas mixture while its backside was polarized at the previously mentioned ϕ values.

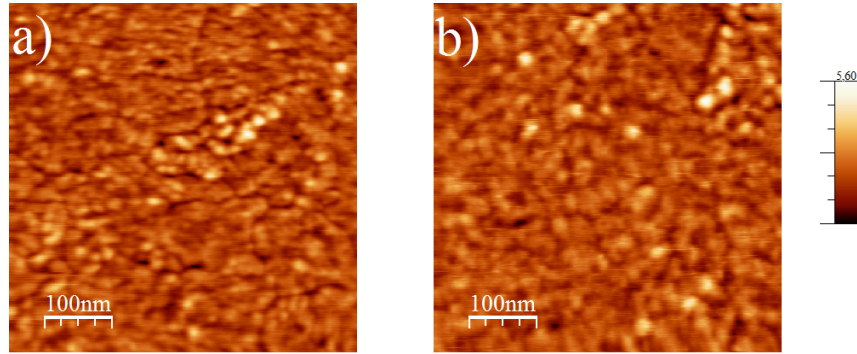


Figure 3.25: AFM image of the SnO_2 sample surface before (a) and after (b) gas exposure while its back was polarized at different ϕ

There are no apparent differences, as both samples look very flat with some small elevations without a recognizable structure. The overall images show a very compact sample with little to no pores on its surface and a rather small grain size. The height histogram for each image can be seen on Figure 3.26. The calculated RMS roughness for sample a) is $R_{rms} = 0,54nm$, while for sample b) is $R_{rms} = 0,56nm$. This difference is within experimental error.

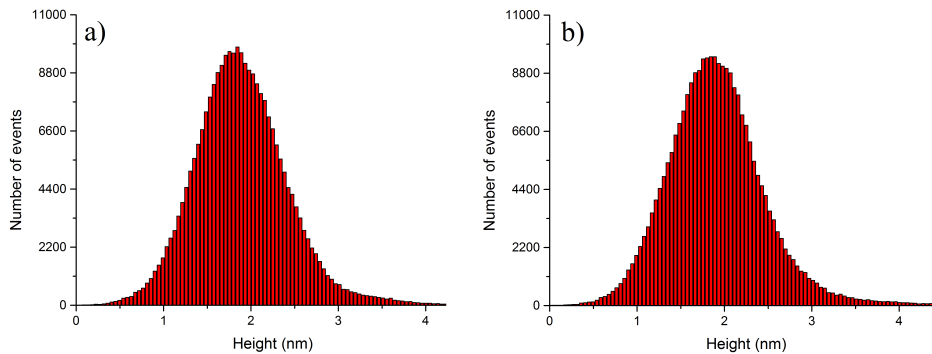


Figure 3.26: Height histogram of a sample before (a) and after (b) gas exposure while its back was polarized at different ϕ

Both histograms have their maximum at around 1.85 nm and are identical in shape, showing that the NO_x adsorption has no noticeable impact on the surface topography.

Chapter 4

Discussion

4.1 Grounding of the surface of the sample

Both the XPS spectra of Sn 3d and the study of the surface grounding performed by measuring the surface potential at various locations via Cu contacts show that the C-shaped contact is not very effective to maintain the surface at zero potential for high values of $|\phi|$. Figure 4.1 shows the highest voltage difference between C-contact and sample surface measured as function of ϕ .

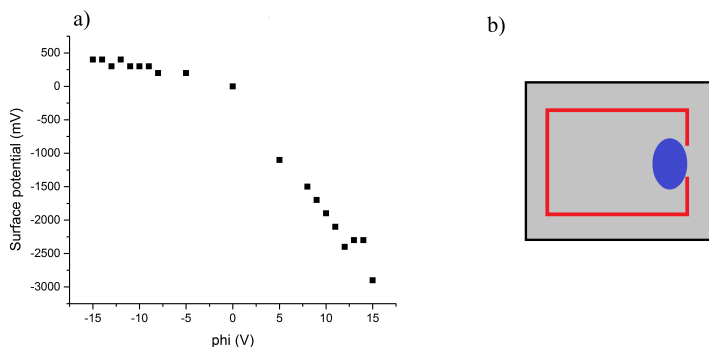


Figure 4.1: **a)** Highest deviation from zero surface potential as function of ϕ . **b)** Point where the highest deviation was found for all ϕ (area marked in blue)

It is worth noticing that all the voltage differences on Figure 4.1 were measured at the same geometrical point: near the aperture of the C-shaped contact (as seen in Figure 4.1 **b**)). At negative backside polarization ϕ , the maximum measured deviation from zero potential is quite low (being at most between 300 and 400 mV for all ϕ values below -8 V) which is in accordance to the observed shift of the entire Sn 3d XPS spectrum of 0,5 eV.

However, when $\phi > 0$, a larger departure from ground potential is measured as compared to its positive counterpart: -900 mV at $\phi = 5V$ and below -1500 mV when $\phi > 10 V$, reaching an extreme of -2800 mV at $\phi = 15V$. This is close to the shift value of 3.3 eV observed in the

Sn 3d spectra when $\phi = 15V$. The 0.5 eV difference may arise due to the different measuring conditions, and to the conductivity change of the SnO_2 in presence of oxygen [1]. Since the impedance of the digital multimeter used is sensibly lower than the impedance expected in a semiconductor non-ohmic juncture, these results are not conclusive (although they do correlate with the observed behavior in the XPS spectra, as previously discussed).

It is concluded that the C-shaped contact is not suitable for proper surface grounding for $\phi > 0$. This behavior may be attributed to a non-ohmic contact such as a Schottky barrier. However, as the reported value for SnO_2 electron affinity is around $\chi = 4,8$ eV [52] and the reported value for Cu work function is between 4,5 and 4,7 eV [53] [54] this should not be the case. In order to properly ground the sample surface, a different contact must be used. Photolithography is widely used in the electronic industry for preparation of contacts having a width and a separation of a few μm or less. By using a mask similar to the sketch in Figure 4.2) it is believed that the surface will be properly grounded while not covering too much of the sample surface. However, it is not clear yet how to proceed, since the surface properties of the semiconductor might be altered during lithography.

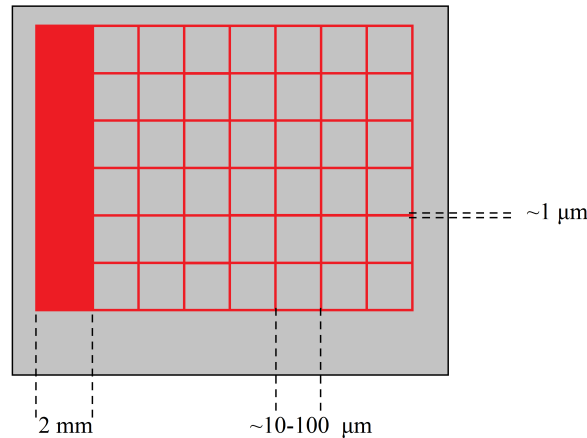


Figure 4.2: Sketch of the proposed grid contact for grounding the surface of the sample

4.2 Argon erosion

If the surface is eroded with an Ar ion beam, it can not be properly grounded even at $\phi = \pm 5$ V. Since the sputtered thickness was quite low (less than 5 nanometers) this hints that the equipotential condition does not depend only on bulk properties, namely the thickness of the sample being around 2 Debye lengths, but also on the properties of the surface itself. There is no suitable explanation for this phenomenon at the moment.

It is possible that by eroding with a lighter ion (such as Ne^+) the equipotential condition can be maintained after erosion (as it would do less damage to the surface)

4.3 QMA

The setup implemented allowed successfully measuring differences in adsorption as a function of the applied voltage. However, it was not possible to observe the desorbed species via mass spectrometry when a potential was applied to the sample. This is believed to be due to the relatively high base pressure on the adsorption chamber, the small amounts of adsorbed species (evidenced by the weak XPS signal) and the low desorption rate. The high pressure is due to the high amounts of water ($\approx 40\%$) present even after baking out the adsorption chamber. Water vapor enters the chamber each time a new sample is introduced, and is released when the higroscopic lead nitrate is heated in order to produce the gas mixture.

The partial pressure change in the XPS chamber produced by the sudden desorption of the adsorbed species on the sample surface should be around 10^{-8} Pa. Since the pressure inside the XPS main chamber was around 10^{-6} Pa, these conditions did not allow to observe rapidly desorbed species with mass spectrometer. In order to properly measure these gases, the base pressure of the chamber must be improved (either via using a cleaner source for the NO_2 or improving the sample insertion method). Another possibility is to replace the standard residual gas analyzer with a close ion source residual gas analyzer, which is able to properly operate at higher base pressures.

4.4 NO_x and H_2O interaction

The calculated mean free path ($\lambda_{fmp} \approx 10^3$ m) of the molecules in the chamber ensure that there is no significant interaction between NO_x species and H_2O in the gaseous phase. Water adsorbs onto the SnO_2 surface [1], and it may be a possible adsorption site of the NO_x species. The sample is exposed to water in the atmosphere, and its surface must be already saturated before the sample is introduced to vacuum. In vacuum, samples normally dry since weakly adsorbed species evaporate from its surface. However, a significant amount of water was detected in the vacuum chamber before exposition (as reported in Table 2.1 on Subsecton 3.1.2), having a partial pressure of $P_{water} \approx 3 \cdot 10^{-6} Pa$. With these values in mind, the mean monolayer formation time was calculated to be around 100 seconds for a sticking coefficient α of 1. Considering this, it is highly likely that the surface does not dry, but instead has a monolayer of adsorbed H_2O before the beginning of the experiment and the adsorption of nitrogen oxides is mediated by water. It is reported by [1] that water forms a monolayer on the (110) SnO_2 in two different configurations. Figure 4.3 shows a sketch of the proposed SnO_2 surface after adsorption and the top view of the two configurations of water molecules onto the surface (when forming a monolayer).

The interaction between NO_2 and H_2O on a metal oxide surface was reported by [42] stating that water might interact with the NO_2 gas in order to produce HNO_4 , which might bond with an oxidized metal onto the metal oxide, further altering the adsorption process. In order to avoid this behavior, a different experiment must be performed with a pure NO_2/O_2 gas mixture from a canister instead of obtaining it from lead nitrate decomposition, so the SnO_2 surface can be safely assumed free of water. If this is the case, the NO species may

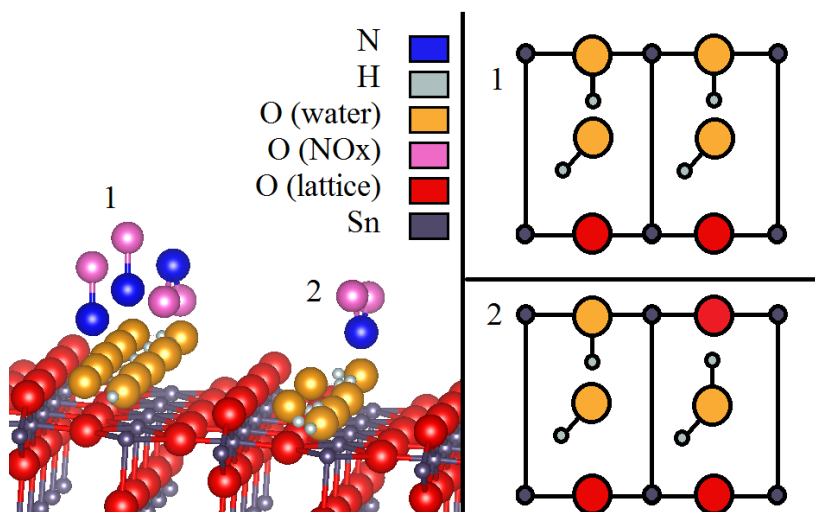


Figure 4.3: Left: This work proposed SnO₂ surface after adsorption of NO_x species. Right: Top view of the two possible configurations for water adsorption on a saturated SnO₂ (110) surface [1].

adsorb to the surface Sn atoms as proposed by [10].

4.5 Adsorption and desorption kinetics

It is corroborated that the desorption is suppressed for positive ϕ values and enhanced by negative ones, as already reported [10]. However, the dependence between the adsorption enhancement/inhibition and the applied potential is not linear: For $|\phi| < 10$ the sample behaves just as if there was no polarization applied to its back. A noticeable change in its adsorption properties is observed for values of $|\phi| = 10$ V and above. This indicates that around $|\phi| = 10$ a threshold polarization value exists. At $\phi = 10$ V and $\phi = -12$ V the expected behavior is inverted.

Due to noise and peak splitting at higher ϕ values, it was not possible to individually identify the behavior of the NO₂ and NO₃, but it was possible to analyze the sum of these signals. At positive back polarization, the relative NO₂+NO₃ concentration increases by around 25% at +15 V (compared to the sum of NO₂ and NO₃ at $\phi = 0$) but decays more quickly at $\tau = 13$ minutes, while for negative back polarization values it decreases by around 30% with a decay time of around 25 minutes. A tentative explanation is that the applied potential modifies only an unstable form of chemisorption, which quickly desorbs when no gas is present. This weak chemisorption is almost completely inhibited by negative polarization.

It is possible to fit the data of the adsorbed species with an exponential function (which comes from the simplest model available for desorption) with a coefficient of determination R^2 which is around 0,85-0,9. In order to properly observe the behavior of the two exponentials presented in equation (1.6), this experiment has to be repeated at different controlled temperatures.

As previously discussed, it was not possible to observe the desorbed gases via mass spectrometry. These desorbed species may be different to the adsorbed NO_x ones, observed via XPS onto the surface: It is reported that gaseous species to a different one when adsorbed, or the adsorption process might yield different gaseous species as byproducts. The work of Rodriguez et. al on Ti [55] shows that adsorbed NO_2 molecules might recombine as NO_3 (which remains on the surface) and gaseous NO (which desorbs).

4.6 Desorption and temperature

As reported in section 3.2, a temperature change in the sample holder was detected after the XPS measurements. This phenomenon introduces a systematic error on the measurements, as the factor that contains the Fermi Energy (the term modified by the potential ϕ) in both Wolkenstein-Geistlinger isotherm at (1.5) and the electroadsorption equation (1.6) is divided by kT , thus introducing a temperature dependence in the experiment. This temperature change is attributed to thermal radiation coming from the x-ray source. Some ways to account for this phenomenon would be to equip the sample holder with a device for in-situ temperature measurement (such as a thermocouple), to include a temperature control device to the insertion arm system in order to heat or cool the sample holder temperature as required. The best way to remove the unwanted heating would be to using a monochromatic x-ray source (which does not directly irradiate the sample, thus avoiding any kind of heating by radiation). Installing both a thermocouple and a device for controlling the temperature of the sampleholder appears to be the best solution, as it both allows the control of the sample temperature and the realization of the experiment previously discussed on section 4.4.

4.7 Thiols on SnO_2

Regarding the tin oxide surface immersed in a thiol solution, the presence of a sulfur signal evidences the adsorption of thiols onto the surface. Since the copper contact was evaporated after the immersion of the sample on the thiol solution, this signal cannot be attributed to a S-Cu bond. It is observed that most of the sulfur is bonded with oxygen, while the amount of S attributed to a thiol-metal bond is rather small (being only a 15% of the total signal). No noticeable changes were observed in the adjustment curves of the XPS sulfur spectra after the application of voltage to the back of the sample, which indicates that sulfur adsorption on tin oxide is not electrically reversible (At least for $\phi = \pm 15$ and below).

Since the binding energy of the S-Cu thiolate is 0.5 eV larger than the one measured for the S-Sn thiolate [56], it should be possible to properly differentiate between thiols bonded to the SnO_2 surface and thiols bonded to Cu. It should also be possible to identify whether the S-Cu bond changes at a given ϕ . With this in mind, a proposed experiment would be to evaporate Cu nanoislands on top of the SnO_2 layer of the MIS sandwich. This can be achieved by evaporating a film of a nominal thickness of 3nm or less. Afterwards, the sample should be submerged in the alkanethiol solution in order to create a monolayer on top. Finally, different backside potentials should be applied to the sample back (probably

larger than 15 V and smaller than -15 V) in order to see if there is a critical ϕ value that induces electrodesorption on the Cu nanoislands.

4.8 TiO₂ film on SnO₂

In the case of the SnO₂ film with a 1 nm TiO₂ layer evaporated on top, it is observed that the behavior of these samples after the application of a backside potential ϕ is different to the samples without the TiO₂ layer. In the case of the TiO₂ covered surfaces, the Sn signal does not split, and the shift observed at $\phi = \pm 15V$ is *smaller* than the one with the non-covered surface. A small peak appears in the Ti 2p spectrum at $\phi = 15V$ (labelled on Figure 3.24 as Ti A) but it cannot be attributed to an ungrounded part of the sample. If this were the case, a similar peak should be observed on the Sn 3d signal around 482,3 eV. These results indicate that the equipotential condition depends on surface properties of the sample which are not described by the Debye length. This is backed up by the observed results after the Ar erosion. This is not yet conclusive, because the electrical properties of the heterojunction depend on the band width, the semiconductor type (n or p) and the position of the Fermi level in both semiconductors, points which were not analyzed in this work.

On the other hand, since the equipotential was maintained, the electroadsorptive effect can be studied on different materials using the same device (depositing different materials on the SnO₂ surface) instead of designing a new one, which would necessarily require the recalculation of a different thickness. Considering this, a proposed experiment is to install a Knudsen cell on the electroadsorption chamber, locating it below the sample holder. In this way, a monolayer of different materials can be reliably evaporated on top of the SnO₂ surface without exposing it to ambient air, thus permitting the study of the electroadsorptive effect on different materials without exposing the sample to air. (reducing the amount of contaminants such as carbon on its surface)

4.9 Future work

Future work should use a dry gas source such a small gas cylinder of commercially prepared mixture (not available in Chile at the moment of this thesis work), as this would help in both reducing contaminants in the gas atmosphere (such as water) and improving the pressure inside the adsorption chamber. This, in turn, may allow the observation of the desorption via mass spectrometer, which should help to determine what species are desorbing. Another way to improve the pressure in the adsorption chamber is to equip it with a small ion pump. A temperature control system should be added in the insertion arm system in order to repeat the experiment at different temperatures. Questions such as the behavior of the sample at $\phi = -10$ V and $\phi = 12$ V and whether the adsorbed species are the same than the desorbed ones could be answered by these measurements. Finding a proper contact geometry that ensures an equipotential surface at high ϕ is also fundamental, as the working principle is that no electric field leaks outside the sample surface.

Conclusion

The quality of the grounding provided by a surface copper C-shaped contact over a thin SnO₂ film forming a metal-insulator-semiconductor structure was tested. It was found that for a positive backside polarization voltage the contact is not appropriate to guarantee proper surface grounding. A grid-like contact would be better for ensuring a proper equipotential on the surface for $\phi > 0$ V.

The surface grounding does not depend exclusively on the bulk properties of the SnO₂ (such as its thickness) but it is also sensitive to its surface characteristics, as the surface equipotential is negatively affected by surface erosion and improved by the deposition of a thin TiO₂ film on top. As such, the relation between thickness and Debye Length is a necessary (but not sufficient) condition of the surface equipotential. A model that includes the surface effect on the equipotential is needed.

A threshold value of $\phi = 10$ V has been found for the electroadsorptive effect in this system. The backside polarization inhibits the adsorption of NO_x species if $\phi < -10$ and promotes it for $\phi > 10$. Two ϕ values which reverse the expected behavior of the device were found at $\phi = 12V$ and $\phi = -10V$.

The characteristic desorption time τ was calculated, and its largest value was found to be larger at $\phi = -15$, and smaller at $\phi = 15$. No further quantitative studies were performed since the recorded spectra were deemed too noisy. This noise does not allow to distinguish between the simplest adsorption model shown in equation (1.4) and the electroadsorptive model presented in equation (1.6). At the moment there is no evidence that backs the previously mentioned electroadsorptive model.

The current setup necessarily saturates the SnO₂ surface with adsorbed water. Despite the reports on the electroadsorptive effect [10] and this thesis work, presently there is no study on the electroadsorptive effect of the mix (NO₂ + O₂) and a clean SnO₂ surface.

Regarding the study of the electroadsorptive effect on a different system, future experiments can be performed on a similar system with either a different surface by evaporating a thin layer of a different material on top of the SnO₂, a surface with a different structure or a functionalized surface with thiols. A combination of these three ideas is also possible, such as observing the electroadsorptive effect on a sample with evaporated Cu nanoislands on its surface.

Bibliography

- [1] M. Batzill and U. Diebold, “The surface and materials science of tin oxide,” *Progress in Surface Science*, vol. 79, no. 2-4, pp. 47–154, 2005.
- [2] T. Wolkenstein, “The electron theory of catalysis on semiconductors.,” *Advances in Catalysis*, vol. 12, pp. 189–264, 1960.
- [3] S. A. Hoenig and J. R. Lane, “Chemisorption of oxygen on zinc oxide.,” *Surface Science*, vol. 11, pp. 163–174, 1968.
- [4] W. Shockley and G. L. Pearson, “Modulation of conductance of thin films of semiconductors by surface charges,” 1948.
- [5] T. Doll, *Advanced gas sensing: The Electroadsorptive Effect and Related Techniques*. Kluwer, Boston, 2003.
- [6] H. Geistlinger, “Electron theory of thin-film gas sensors,” *Sensors and Actuators B*, vol. 17, pp. 47–60, 1993.
- [7] J. Velasco-Velez, U. Kunze, T. Haas, and T. Doll, “Co-adsorption processes, kinetics and quantum mechanical modelling of nanofilm semiconductor gas sensors,” *Phys. Status Solidi A*, vol. 207, no. 4, pp. 924–929, 2010.
- [8] W. Hellmich, G. Müller, C. B. v. Braunmühl, T. Doll, and I. Eisele, “Field-effect-induced gas sensitivity changes in metal oxides,” *Sensors and actuators B*, vol. 43, pp. 132–139, 1997.
- [9] K. Scharnagl, M. Bögner, A. Fuchs, R. Winter, T. Doll, and I. Eisele, “Enhanced room temperature gas sensing with metal oxides by means of the electroadsorptive effect in hybrid suspended gate fet,” *Phys. Status Solidi B*, vol. 207, no. 4, pp. 924–929, 2010.
- [10] T. Doll, J. Velasco-Velez, D. Rosenthal, J. Avila, and V. Fuenzalida, “Direct observation of the electroadsorptive effect on ultrathin films for microsensor and catalytic-surface,” *ChemPhysChem*, vol. 14, no. 11, pp. 2505–2510, 2013.
- [11] M. Noked, E. Avraham, A. Soffer, and D. Aurbach, “The rate-determining step of electroadsorption processes into nanoporous carbon electrodes related to water desalination,” *J. Phys Chem. C*, vol. 113, pp. 21319–21327, 2009.

- [12] Z. Wang, “Nanobelts, nanowires, and nanodiskettes of semiconducting oxides—from materials to nanodevices,” *Advanced Materials*, vol. 15, no. 5, p. 432, 2003.
- [13] A. Maiti, J. A. Rodriguez, M. Law, P. Kung, J. R. McKinney, and P. Yang, “SnO₂ nanoribbons as NO₂ sensors: Insights from first principles calculations,” 2003.
- [14] H. Witschi, “Ozone, nitrogen dioxide and lung cancer: A review of some recent issues and problems,” *Toxicology*, vol. 48, no. 1, pp. 1–20, 1988.
- [15] N. O. Savage, S. A. Akbar, and P. K. Dutta, “Titanium dioxide based high temperature carbon monoxide selective sensor,” vol. 72.
- [16] U. Weimar and W. Göpel, “A.c measurements on tin oxide sensors to improve selectivities and sensitivities,” vol. 26.
- [17] A. Dieguez, A. Romano-Rodriguez, A. Vila, and J. Morante, “The complete Raman spectrum of nanometric SnO₂ particles,” vol. 90, no. 3.
- [18] A. Many, Y. Goldstein, and N. Grover, *Semiconductor Surfaces*. North-Holland, Amsterdam, 1965.
- [19] P. Weisz, “Effects of electronic charge transfer between adsorbate and solid on chemisorption and catalysis,” *J. Chem. Phys.*, vol. 21, no. 11, p. 1531, 1954.
- [20] T. Seiyama, A. Kato, K. Fujiishi, and M. Nagatani, “A new detector for gaseous components using semiconductive thin films.,” *Analytical Chemistry*, vol. 34, no. 11, pp. 1502–1503, 1962.
- [21] T. Doll, *Advanced Gas Sensing: The Electroadsorptive Effect and Related Techniques*. Kluwer, Boston, 2003.
- [22] N. Barsan and U. Weimar, “Conduction model of metal oxide gas sensors,” *Sensors and Actuators B*, vol. 17, pp. 47–60, 1993.
- [23] C. Wang, L. Yin, L. Zhang, D. Xiang, and R. Gao, “Metal oxide gas sensors: Sensitivity and influencing factors.,” *Sensors*, vol. 10, pp. 2088–2106, 2010.
- [24] S. Samson and C. G. Fonstad, “Defect structure and electronic donor levels in stannic oxide crystal,” *J. Appl. Phys.*, vol. 44, pp. 4618–4621, 1973.
- [25] F. J. Arlinghaus, “Energy bands in stannic oxide,” *Journal of Physics and Chemistry of Solids*, vol. 35, pp. 931–935, 1974.
- [26] K. J. Button, C. G. Fonstad, and W. Dreybrodt, “Determination of the electron masses in stannic oxide by submillimeter cyclotron resonance,” *Physical Review B*, vol. 4, no. 12, 1971.
- [27] A. M. Ganose and D. O. Scanlon, “Band gap and work function tailoring of SnO₂ for improved transparent conducting ability in photovoltaics,” *J. Mater. Chem. C*, vol. 4,

- pp. 1467–1475, 2016.
- [28] A. W. Adamson and A. P. Gast, *Physical Chemistry of Surfaces*. Wiley-Interscience, New York, 1997.
- [29] C. Nicosia and J. Huskens, “Reactive self-assembled monolayers: from surface functionalization to gradient formation,” *Mater. Horiz.*, vol. 1, pp. 32–45, 2014.
- [30] U. Carragher, *An Electrochemical Investigation into the Corrosion Protection Properties of Coatings for the Active Metal Copper*. PhD thesis, National University of Ireland.
- [31] J.-B. D. Green, M. T. McDermott, and M. D. Porter, “Nanometer-scale mapping of chemically distinct domains at well-defined organic interfaces using frictional force microscopy,” *J. Phys. Chem.*, vol. 99, pp. 10960–10965, 1995.
- [32] B. Zhang, T. Kong, W. Xu, R. Su, Y. Gao, and G. Cheng, “Surface functionalization of zinc oxide by carboxyalkylphosphonic acid self-assembled monolayers,” *Langmuir*, vol. 4, pp. 1467–1475, 2010.
- [33] Z. Petrovic, J. Katic, M. Metikos-Hukovic, H. Dadafarin, and S. Omanovic, “Modification of a nitinol surface by phosphonate self-assembled monolayers,” *Mater. Horiz.*, vol. 1, pp. 32–45, 2014.
- [34] Y. Chang, C. Ukiwe, and D. Y. Kwok, “Chain length effect of alkanethiol self-assembled monolayers on the maximum spreading ratio of impacting water droplets,” *Colloids and Surfaces A: Physicochem. Eng. Aspects*, vol. 260, pp. 255–263, 2005.
- [35] S. Donoso, “Oxidación de películas delgadas de cobre recubiertas con dodecanetiol,” Master’s thesis, Universidad de Chile, 2013.
- [36] M. R. Shadnam and A. Amirfazli, “Kinetics of alkanethiol monolayer desorption from gold in air,” *Chem. Commun.*, pp. 4869–4871, 2005.
- [37] J. F. Moulder, W. F. Stickle, P. E. Sobol, and K. D. Bomben, *UHV AFM/STM User’s Guide*. OMICRON NanoTechnology, 2002.
- [38] T. L. Alford, L. C. Feldman, and J. W. Mayer, *Fundamentals of nanoscale film analysis*. Springer, 2007.
- [39] G. Acosta, “Formación de capas moleculares en superficies.”
- [40] I. Horcas, R. Fernandez, J. Gomez-Rodriguez, J. Colchero, J. Gomez-Herrero, and A. M. Baro, “WSXM: A software for scanning probe microscopy and a tool for nanotechnology,” *Rev. Sci. Instrum.*, vol. 78, p. 03705, 2007.
- [41] V. Fuenzalida, “Análisis de la señal au 4f en función de la energía de paso.”
- [42] J. Baltrusaitis, P. M. Jayaweeraa, and V. H. Grassian, “XPS study of nitrogen dioxide adsorption on metal oxide particle surfaces under different environmental conditions.”

Physical Chemistry Chemical Physics, vol. 11, pp. 8295–8305, 2009.

- [43] J. F. Moulder, W. F. Stickle, P. E. Sobol, and K. D. Bomben, *Handbook of X-Ray Photoelectron Spectroscopy*. Perkin-Elmer Corporation Physical Electronics Division, 1992.
- [44] C. Vinod, J. N. Hansa, and B. Nieuwenhuys, “Interaction of small molecules with au(3 1 0): Decomposition of no.,” *Applied Catalysis. A, General*, vol. 291, no. 1-2, pp. 93–97, 2005.
- [45] A. Bukhtiyarov, R. Kvon, A. Nartova, I. Prosvirin, and V. Bukhtiyarov, “In-situ XPS investigation of nitric oxide adsorption on (111), (310), and (533) gold single crystal faces.,” *Surface Science*, vol. 606, pp. 559–563, 2012.
- [46] N. Hellgren, J. Guo, Y. Luo, C. S  the, A. Aguid, S. Kashtanov, J. Nordgren, H.   gren, and J.-E. Sundgren, “Electronic structure of carbon nitride thin films studied by X-ray spectroscopy techniques.,” *Thin Solid Films*, vol. 471, pp. 19–34, 2005.
- [47] W. Zheng, K. Xing, N. Hellgren, M. L  gdlund,   . Johansson, U. Gelivs, W. Salaneck, and J.-E. Sundgren., “Nitrogen 1s electron binding energy assignment in carbon nitride thin films with different structures.,” *Journal of Electron Spectroscopy and Related Phenomena*, vol. 87, pp. 45–49, 1997.
- [48] M. Dubey, S. L. Bernasek, and J. Schwartz, “Highly sensitive nitric oxide detection using X-ray photoelectron spectroscopy,” vol. 129.
- [49] Y. W. Yang and L. J. Fan, “High-Resolution XPS study of Decanethiol on Au(111): Single Sulfur-Gold Bonding Interaction,” *Langmuir*, vol. 18, pp. 1157–1164, 2002.
- [50] C. Yan, M. Zharnikov, A. G  lzha  user, , and M. Grunze, “Preparation and characterization of self-assembled monolayers on indium tin oxide,” *Langmuir*, vol. 16, pp. 6208–6215, 2000.
- [51] M. Sevilla and A. B. Fuentes, “Highly porous S-Doped carbons.,” *Microporous and Mesoporous Materials*, vol. 158, pp. 318–323, 2011.
- [52] Y. Cheng, R. Yang, J.-P. Zheng, Z. L. Wang, and P. Xiong, “Characterizing individual SnO₂ nanobelt field-effect transistors and their intrinsic responses to hydrogen and ambient gases,” *Mater. Chem. Phys.*, vol. 137, pp. 372–380, 2012.
- [53] P. A. Anderson, “The Work Function of Copper,” vol. 76, no. 3.
- [54] W. Li and D. Y. Li, “On the correlation between surface roughness and work function in copper,” *J. Chem. Phys.*, vol. 122, pp. 388–390, 2005.
- [55] J. A. Rodriguez, T. Jirsak, G. Liu, J. Hrbek, J. Dvorak, and A. Maiti, “Chemistry of NO₂ on oxide surfaces: Formation of NO₃ on TiO₂ and NO₂ ↔ O vacancy interactions,” *J. Am. Chem. Soc.*, vol. 123, pp. 9597–9605, 2001.

- [56] M. Zharnikov, “High-resolution X-ray photoelectron spectroscopy in studies of self-assembled organic monolayers,” *Journal of Electron Spectroscopy and Related Phenomena*, vol. 178-179, pp. 380–393, 2010.
- [57] T. Wolkenstein, *Electronic Processes on Semiconductor Surfaces during Chemisorption*. Consultants Bureau, New York, 1991.
- [58] Y. Wang, J. Im, J. W. Soares, D. M. Steeves, and J. E. Whitten, “Thiol adsorption on and reduction of copper oxide particles and surfaces.,” *Langmuir*, vol. 16, pp. 3848–3857, 2016.
- [59] Y. Kanaya, R. Cao, H. Akimoto, M. Fukuda, Y. Komazaki, Y. Yokouchi, M. Koike, H. Tanimoto, N. Takegawa, and Y. Kondo, “Urban photochemistry in central Tokyo: 1. Observed and modeled OH and HO₂ radical concentrations during the winter and summer of 2004,” *Journal of Geophysical Research*, vol. 112, no. D21312, 2007.